Semiconductor Materials and Devices Series

Semiconductor Nanostructures for Optoelectronic Applications

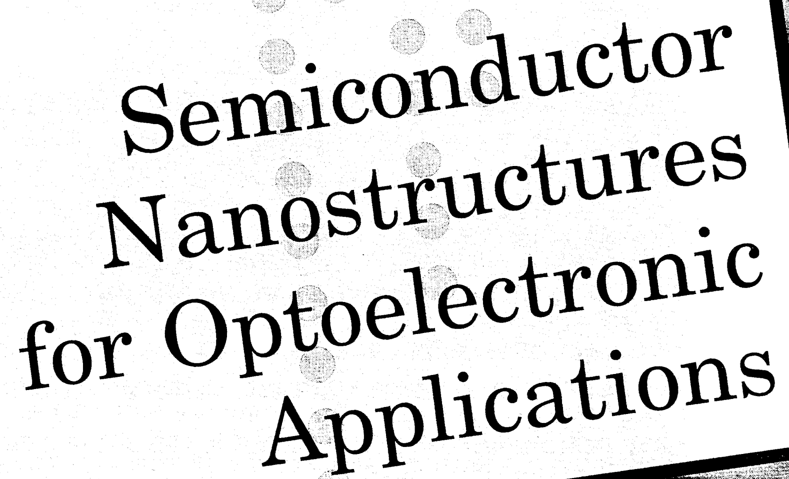

Todd Steiner, *editor*

Semiconductor Nanostructures for Optoelectronic Applications

Todd Steiner

Editor

Artech House, Inc.
Boston • London
www.artechhouse.com

Library of Congress Cataloging-in-Publication Data

A catalog record of this book is available from the U.S. Library of Congress.

British Library Cataloguing in Publication Data

Semiconductor nanostructures for optoelectronic applications
—(Artech House semiconductor materials and devices library)
1. Semiconductors 2. Nanostructured materials 3. Optoelectronic devices
I. Steiner, Todd
621.3'8152

ISBN 1-58053-751-0

Cover design by Gary Ragaglia

© 2004 ARTECH HOUSE, INC.
685 Canton Street
Norwood, MA 02062

All rights reserved. Printed and bound in the United States of America. No part of this book may be reproduced or utilized in any form or by any means, electronic or mechanical, including photocopying, recording, or by any information storage and retrieval system, without permission in writing from the publisher.

All terms mentioned in this book that are known to be trademarks or service marks have been appropriately capitalized. Artech House cannot attest to the accuracy of this information. Use of a term in this book should not be regarded as affecting the validity of any trademark or service mark.

International Standard Book Number: 1-58053-751-0

10 9 8 7 6 5 4 3 2 1

Contents

CHAPTER 1

Introduction 1

1.1 Synopsis 1
1.2 Growth 1
1.3 Optoelectronic Devices Based on Semiconductor Nanostructures 2
1.4 Materials for Semiconductor Nanostructures 2
1.5 Summary 3

CHAPTER 2

Review of Crystal, Thin-Film, and Nanostructure Growth Technologies 5

2.1 Introduction 5
2.2 Review of Thermodynamics 6
  2.2.1 Chemical Reactions 7
  2.2.2 Phase Diagrams 7
2.3 Bulk Crystal Growth Techniques 8
  2.3.1 Czochralski Method 8
  2.3.2 Bridgman Method 11
  2.3.3 Float-Zone Method 13
  2.3.4 Lely Growth Methods 14
2.4 Epitaxial Growth Techniques 16
  2.4.1 Liquid Phase Epitaxy 16
  2.4.2 Vapor Phase Epitaxy 17
  2.4.3 Molecular Beam Epitaxy 20
  2.4.4 Metalorganic Chemical Vapor Deposition 24
  2.4.5 Atomic Layer Epitaxy 29
2.5 Thin-Film Deposition Techniques 29
  2.5.1 Plasma-Enhanced Chemical Vapor Deposition 29
  2.5.2 Vacuum Evaporation 31
  2.5.3 Sputtering 33
2.6 Growth of Nanostructures 34
  2.6.1 Properties and Requirements of Quantum Dot Devices 35
  2.6.2 Growth Techniques 36
  References 41

CHAPTER 3

Quantum Dot Infrared Photodetectors 45
3.1 Introduction 45
3.2 QD and QDIP Structure Growth and Characterization 49
3.2.1 GaAs Capped Large and Small InAs QDs 50
3.2.2 AlGaAs Capped Large InAs MQD QDIP Structures 57
3.2.3 $In_xGa_{1-x}As$ Capped Small and Large InAs MQD-Based QDIP Structures 64
3.3 QDIP Device Characteristics 76
3.3.1 Device Structures 76
3.3.2 Unintentionally Doped Large (PIG) InAs/GaAs MQD-Based Detectors 77
3.3.3 QDIPs with AlGaAs Blocking Layers 87
3.3.4 InAs/InGaAs/GaAs QDIPs 92
3.3.5 Dual-Color QDIPs 102
3.4 Prognosis 107
Acknowledgments 109
References 109

CHAPTER 4

Quantum Dot Lasers: Theoretical Overview 113
4.1 Introduction: Dimensionality and Laser Performance 113
4.2 Advantages of an Idealized QD Laser 115
4.3 Progress in Fabricating QD Lasers 115
4.4 State-of-the-Art Complications 116
4.4.1 Nonuniformity of QDs 117
4.4.2 Parasitic Recombination Outside QDs 126
4.4.3 Violation of Local Neutrality in QDs 129
4.4.4 Excited States 131
4.4.5 Spatial Discreteness of Active Elements: Hole Burning 132
4.4.6 Intrinsic Nonlinearity of the Light-Current Characteristic 134
4.4.7 Critical Sensitivity to Structure Parameters 139
4.4.8 Dependence of the Maximum Gain on the QD Shape 142
4.4.9 Internal Optical Loss 143
4.5 Novel Designs of QD Lasers with Improved Threshold and Power Characteristics 148
4.5.1 Temperature-Insensitive Threshold 148
4.5.2 Enhanced Power Performance 150
4.6 Other Perspectives 151
References 153

CHAPTER 5

High-Speed Quantum Dot Lasers 159

5.1 Introduction 159

5.2 MBE Growth of Self-Organized QDs and Their Electronic Properties 160

5.2.1 Self-Organized Growth of In(Ga)As QDs 160

5.2.2 Electronic Spectra of In(Ga)As/GaAs QDs 161

5.3 Separate Confinement Heterostructure QD Lasers and Their Limitations 163

5.3.1 Carrier Relaxation and Phonon Bottleneck in Self-Organized QDs 164

5.3.2 Hot Carrier Effects in SCH QD Lasers 167

5.4 Tunnel Injection of Carriers in QDs 168

5.4.1 Tunneling-Injection Laser Heterostructure Design and MBE Growth 169

5.4.2 Measurement of Phonon-Assisted Tunneling Times 170

5.5 Characteristics of High-Speed Tunneling-Injection QD Lasers 172

5.5.1 Room Temperature DC Characteristics 172

5.5.2 Temperature-Dependent DC Characteristics 172

5.5.3 High-Speed Modulation Characteristics 174

5.6 Conclusion 183

Acknowledgments 183

References 183

CHAPTER 6

Zinc Oxide-Based Nanostructures 187

6.1 Introduction 187

6.1.1 General Properties of ZnO 187

6.1.2 ZnO One-Dimensional Nanostructures 189

6.2 Growth Techniques 191

6.2.1 Growth Mechanisms 191

6.2.2 Growth Techniques 194

6.2.3 Summary 210

6.3 Characterizations 211

6.3.1 Structural Characterizations 211

6.3.2 Optical Characterizations 215

6.4 Device Applications 219

6.4.1 Optical Devices 219

6.4.2 Electronic Devices 221

References 224

CHAPTER 7

Antimony-Based Materials for Electro-Optics 229

7.1 Introduction 229
7.1.1 Antimony 229
7.1.2 Sb-Based III-V Semiconductor Alloys 230
7.1.3 Bulk Single-Crystal Growth 232
7.1.4 Applications 232
7.2 III-Sb Binary Compounds: GaSb, AlSb, and InSb 235
7.2.1 GaSb 235
7.2.2 AlSb 239
7.2.3 InSb 242
7.3 InAsSb 250
7.3.1 Physical Properties 250
7.3.2 Growth of InAsSb 253
7.3.3 Characterizations 253
7.3.4 Device Measurement 256
7.4 InTlSb 259
7.4.1 MOCVD Growth of InTlSb 259
7.4.2 InTlSb Photodetectors 262
7.5 InBiSb 262
7.5.1 MOCVD Growth of InSbBi 262
7.5.2 InSbBi Photodetectors 265
7.6 InTlAsSb 266
7.7 InAsSb/InAsSbP for IR Lasers 267
7.7.1 Growth and Characterization of InAsSb and InAsSbP 268
7.7.2 Strained-Layer Superlattices 269
7.7.3 Device Results 271
7.8 GaSb/InAs Type II Superlattice for IR Photodetectors 273
7.8.1 Introduction 273
7.8.2 Experimental Results for Type II Photodetectors 275
Acknowledgments 284
References 285

CHAPTER 8

Growth, Structures, and Optical Properties of III-Nitride Quantum Dots 289

8.1 Introduction 289
8.2 Growth of III-Nitride QDs 291
8.2.1 MBE Growth of III-Nitride QDs 292
8.2.2 Other Techniques 314
8.3 Optical Properties of III-Nitride QDs 317
8.3.1 Effects of Quantum Confinement, Strain, and Polarization 318

229
229
229
230
232
232
235
235
239
242
250
250
253
253
256
259
259
262
262
262
265
266
267
268
269
271
273
273
275
284
285

289
289
291
292
314
317
318

8.3.2 GaN QDs 323
8.3.3 InGaN QDs 337
8.4 Summary 343
References 344

CHAPTER 9

Self-Assembled Germanium Nano-Islands on Silicon and Potential Applications 349

9.1 Introduction 349
9.2 Heteroepitaxy Mechanisms 349
9.3 Uniform Ge Islands 350
9.4 Registration and Regimentation of Ge Islands 355
9.5 Novel Device Applications 362
9.5.1 Optoelectronics 362
9.5.2 Thermoelectricity 365
9.5.3 Electronics Applications 366
9.5.4 Quantum Information Applications 366
9.6 Conclusion 367
References 367

CHAPTER 10

Carbon Nanotube Engineering and Physics 371

10.1 Introduction 371
10.2 Controlled Fabrication of Uniform Nanotubes in a Highly Ordered Array 373
10.3 Interfacing with Biomolecules and Cells 379
10.4 Intrinsic Quantum Electromechanical Couplings 382
10.5 Extrinsic Coupling to Radiation Fields 391
10.6 Heterojunction Nanotubes 392
10.7 Prospects for Future Advances 396
Acknowledgments 398
References 398

Acronyms 403
About the Editor 407
Index 409

CHAPTER 1

Introduction

Todd Steiner, Air Force Office of Scientific Research

1.1 Synopsis

As we begin the twenty-first century, nanoscience and technology are advancing at a rapid pace and making revolutionary contributions in many fields including electronics, materials science, chemistry, biology, structures and mechanics, and optoelectronics. Although nanoscience and technology are progressing along many fronts, the most impressive progress has been made in the area of semiconductor technology. This book reviews recent progress in semiconductor nanostructure growth and materials development and also reviews progress in semiconductor devices using nanostructures, with a particular emphasis on 3D nanostructures that have emerged during the last 10 years.

1.2 Growth

Semiconductor nanostructures have been enabled by the advancements in epitaxial growth techniques, which are now capable of growing epilayers as thin as one atomic layer and with interface roughnesses that are a mere fraction of a monolayer. The development of advanced crystal and thin-film growth technologies capable of realizing high crystalline quality and purity of materials is an enabling step in bringing semiconductor devices to reality. These growth techniques are reviewed in Chapter 2. Chapter 2 starts with an overview of the bulk crystal growth techniques that are required for obtaining high-quality substrates, then looks at the primary means for producing high-quality epilayers, including liquid phase epitaxy, vapor phase epitaxy, molecular beam epitaxy, *metalorganic chemical vapor deposition* (MOCVD), and *atomic layer epitaxy* (ALE), as well as techniques for thin-film deposition including plasma-enhanced chemical vapor deposition, electron cyclotron resonance, vacuum evaporation, and sputtering. Chapter 2 then discusses the different growth modes of low-dimensional structures such as quantum wires and quantum dots.

1.3 Optoelectronic Devices Based on Semiconductor Nanostructures

Since the successful development of quantum well lasers in the 1970s, one of the richest areas of application of semiconductor nanostructures has been in the area of optoelectronic devices, with the two most important areas being semiconductor lasers and detectors. Early efforts focused on band-to-band transitions and have progressed more recently to intersubband devices. In addition, the early devices utilized 2D nanostructures, either superlattices or quantum wells. In recent years, the growth of quantum dots and their integration into working devices has revolutionized semiconductor devices. This book highlights results in semiconductor devices based on *quantum dots* (QDs).

In Chapter 3, we review progress on *quantum dot infrared detectors* (QDIPs) by providing a comprehensive discussion of the growth, structural and optical characterization, and device figures of merit. We discuss the QD and the QDIP structure growth, QD size distribution, and the tailoring of the QD electronic energy levels and wave functions via manipulation of the QD confinement potential. We also show how to take advantage of stress manipulation to realize multiple-color QDIPs. One section focuses on the QDIP device characteristics (dark current, responsivity, noise, photoconductive gain, detectivity) for each of three classes of QDIPs discussed: InAs/GaAs/AlGaAs, InAs/InGaAs/GaAs, and dual-color InAs/InGaAs/GaAs QDIPs.

In Chapter 4, we provide a theoretical overview of QD lasers, including the advantages of QD lasers over quantum well lasers, the recent progress in fabricating QD lasers, and a theoretical treatment of many issues of practical importance in developing QD lasers, such as the nonuniformity of QDs, parasitic recombination outside of QDs, threshold and power characteristics, and nonlinear properties. The chapter also includes novel designs for QD lasers with improved threshold and power characteristics.

In Chapter 5, we provide an overview of InGaAs tunnel injection QD lasers, which have demonstrated the lowest thresholds for QD lasers and the highest modulation bandwidths. This chapter describes the growth of these QD lasers, the unique carrier dynamics observed in self-organized QDs, their effect on high-frequency performance of QD lasers, and the novel injection technique whereby electrons are injected into the QD ground state by tunneling. The enhanced performance of these tunnel injection QD lasers is also described and discussed.

1.4 Materials for Semiconductor Nanostructures

Progress in semiconductor nanostructures is advancing to a wide variety of material systems. In this book we highlight the progress in five important material systems of technological importance. Each of these material systems has demonstrated 2D and 3D nanostructures and has had varying degrees of success in the fabrication of optoelectronic devices.

In Chapter 6 we review progress in zinc oxide-based nanostructures, including the Zno/ZnMgO system. Zinc oxide is emerging as an important material for

ultraviolet and visible optoelectronic applications, due to the ease with which light emission can be obtained. In Chapter 7 we review progress in antimony-based nanostructures, including the binary compounds GaSb, InSb, and AlSb; the tertiary compounds InAsSb, InAsP, InTlSb, and InSbBi; and the quaternary compounds InTlAsSb and InAsSbP. Devices based on these materials are also discussed. In Chapter 8 we review recent advances in the growth of III-nitride quantum dots and their unique properties. The growth techniques and the structural and optical properties associated with quantum confinement, strain, and polarization in GaN and $In_xGa_{1-x}N$ quantum dots are discussed in detail.

In Chapter 9 we review the progress of nanostructures in the silicon/germanium material system, which has the potential for bringing optoelectronics and photonics to silicon. Specifically, we review issues of Ge island formation on Si. We show uniform Ge island formation on planar Si and ordered island formation on prepatterned mesa structures. We discuss the effect of growth conditions such as growth temperature, deposition rate, deposition coverage, and substrate patterning on the formation of the islands. We discuss the potential applications of Ge islands in the fields of optoelectronics, thermoelectricity, electronics, and quantum information. In Chapter 10, we present a review of carbon nanotubes, especially for optoelectronics applications. The field of carbon nanotubes has advanced quickly and widely on many fronts during the past decade. Controlled fabrication of carbon nanotubes of uniform diameter, length, and spacing is now feasible. Real and perceived potential applications in electronics, sensing, molecular biology, actuation, composite material, and energy storage have been demonstrated. We introduce some of these advances and some of the fundamental properties of the carbon nanotubes, discuss the underlying physics of new effects and phenomena observed or anticipated, and describe the controllable fabrication processes of new forms of nanotubes, as well as some interesting and relatively new and unconventional directions of potential applications.

1.5 Summary

As we enter the twenty-first century, semiconductor nanostructures are revolutionizing many areas of electronics, optoelectronics, and photonics. We present in this volume some of the more interesting results that are leading the revolution in the area of optoelectronics. It is in this area that the real benefits of 3D structures are being realized for practical devices. These achievements will serve to enhance the contributions of semiconductor nanostructures in other areas, helping to maintain the leading position of semiconductor nanotechnology in the more general world of nanoscience and technology.

CHAPTER 4

Quantum Dot Lasers: Theoretical Overview

Levon V. Asryan and Serge Luryi, State University of New York at Stony Brook

4.1 Introduction: Dimensionality and Laser Performance

The emergence of devices based on nanometer-size active elements marked the era of nanoelectronics and nanophotonics. Among such elements are notably low-dimensional heterostructures, such as QWs [1], *quantum wires* (QWRs) [2], and QDs [3]. Quantum confinement in low-dimensional heterostructures strongly modifies the basic properties of a semiconductor crystal.

In a QW, carriers are spatially confined in the transverse direction and move freely in its plane. In a QWR, carriers are spatially confined in two transverse directions and move freely along it. Hence, the carrier energy spectra in both QWs and QWRs are continuous within wide subbands of allowed states and, in this sense, they do not qualitatively differ from those in a bulk crystal.

In a QD, carriers are three-dimensionally confined and the modification of electronic properties is most strongly pronounced: the energy levels are discrete. For this reason, QDs are also referred to as *superatoms* or artificial atoms. A QD of typical size (several nanometers to several tens of nanometers) contains several thousands to several tens of thousands atoms. Quantum dots have generated much interest as a new class of human-made materials with tunable (by varying both the composition and size) energies of discrete atomic-like states.

The semiconductor laser is the fundamental device of modern optoelectronics and photonics. It was proposed long ago [4] that reducing the dimensionality of the active region could significantly improve laser performance due to the quantum-size effect. This general idea was initially applied to QW lasers [5–7] and by now QW lasers have replaced bulk lasers in most commercial applications [1]. Further enhancement is expected for lasers with lower dimensionality, such as QWR and especially QD lasers. In the context of QWR and QD lasers, this idea was first analyzed theoretically in [8]. Due to a continuous density of states within allowed subbands, using QWs and QWRs as an active medium for stimulated optical transitions can only quantitatively enhance device characteristics compared to those of a bulk device [9, 10].

4.2

Figure 4.1 shows the transformation of the density of states and the schematic gain spectrum with the reduction in the dimension of the active region. As the density of states narrows, one needs smaller number of states to be filled to attain transparency of the active region and the lasing. As a result, both the transparency current (injection current required for zero gain) and the threshold current (current, at which the gain equals the loss and the lasing starts) decrease, and also their temperature dependences become less pronounced. Lowering the threshold current and improving its temperature stability are important objectives in the development of diode lasers [11]. As seen from the figure, the radical, qualitative change in the density of states and the gain spectrum occurs only in QDs. The discrete carrier spectrum in QDs appears therefore ideally suitable for lasing generation with low threshold and high temperature stability. Thus, the semiconductor (diode) QD lasers form a novel class of injection lasers that promise radically enhanced

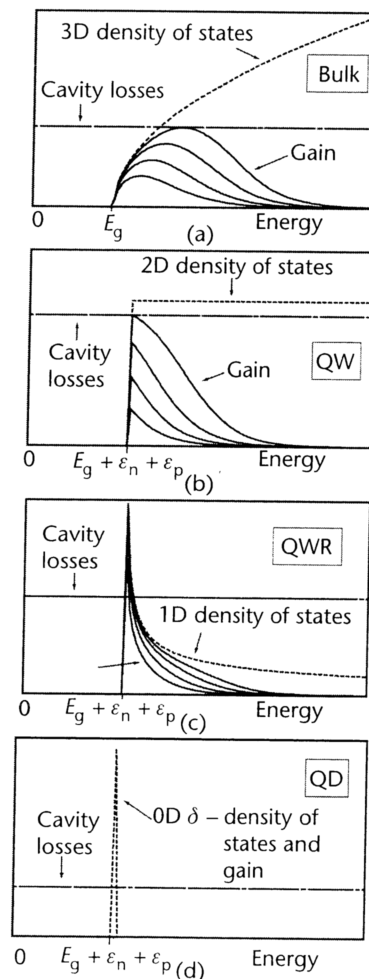

Figure 4.1 (a–d) Transformation of the density of states and the schematic gain spectrum for different dimensions of an active region.

4.2

4.3

operating characteristics [3, 8, 12–14]. The use of QDs as an active medium in injection lasers is a dramatic example of nanotechnology applied to devices of high commercial interest.

4.2 Advantages of an Idealized QD Laser

The principal advantages of QD lasers over the conventional QW lasers can be summarized as follows:

- Significantly lower threshold current density;
- Significantly weaker temperature dependence of the threshold current, ideally, temperature-insensitive threshold current;
- Superior opportunity for tuning the gain spectrum width and the emission wavelength (color of light);
- Low chirp (shift of the lasing wavelength with injection current), ideally, zero α-factor.

In the ongoing improvement of semiconductor lasers, each of the above areas has always been on the high-priority list and motivated the very idea of heterostructure lasers [15]. The low threshold currents of heterostructure lasers, already demonstrated during the early stage of development [16–18], provided much momentum for continuing research in this field.

4.3 Progress in Fabricating QD Lasers

Practical realization of the advantages of QD lasers became possible with the advent of QD structures with high uniformity of size and shape.

Initial attempts to fabricate QDs and QD devices relied on the traditional—at the time—means, such as selective etching of QW structures or QW intermixing, growth on profiled substrates and on cleavage facets, or condensation in glassy matrices [19]. These efforts, however, did not produce device-oriented structures.

A breakthrough in fabricating QD lasers (first optically pumped [20] and then current injected [21]) came with the use of self-organizing effects in heteroepitaxial systems. The nonplanar 3D growth, which had been traditionally considered undesirable, has led to the direct formation of QDs. The possibility of forming 3D islands in a wideband matrix was first demonstrated in [22]. At the time, however, this did not attract much attention because the prospect of fabricating uniform QDs looked doubtful. It took extensive experimental and theoretical studies [23] before QD arrays of high structural perfection and uniformity could be realized in practice.

Today, we have a reasonably mature epitaxial growth technology that employs spontaneous formation of semiconductor nanostructures in heteroepitaxial mismatched systems. This technology allows us to control both the surface density and the size of QDs [24]. The most extensively studied heterosystems for QD lasers are InAs/GaAs, InAs/InGaAs, InGaAs/GaAs, and InGaAs/AlGaAs on the GaAs

substrate. Using these material systems, one can vary the lasing wavelength in the wide spectral range from 0.87 to 1.9 μm, including 1.3 and 1.55 μm, the most desirable wavelengths for telecommunication applications. The use of GaInP/InP and InAlAs/GaAs QDs extended the range into the visible (red) spectrum.

Commercial perspectives on QD lasers have stimulated the efforts of many groups and led to significant progress in fabrication technology. Among the demonstrated advantages of QD lasers is the lowest threshold current density—19 A/cm^2—ever reported for *continuous-wave* (CW) room temperature operation for semiconductor lasers of any type [25]. A temperature stability of the threshold current that is superior to QW lasers has been demonstrated; a characteristic temperature T_0 above 150K was reported at operating temperatures well above room temperature [26–28]. Wide spectral tunability has also been demonstrated [29].

4.4 State-of-the-Art Complications

Figure 4.2 shows schematically the cross section and the band diagram of a typical QD laser. The bipolar device employs stimulated transitions between the quantized energy levels of electrons and holes in QDs. In this section, we focus on the most important issues that hinder the development of such lasers with superior performance compared to other contemporary semiconductor lasers.

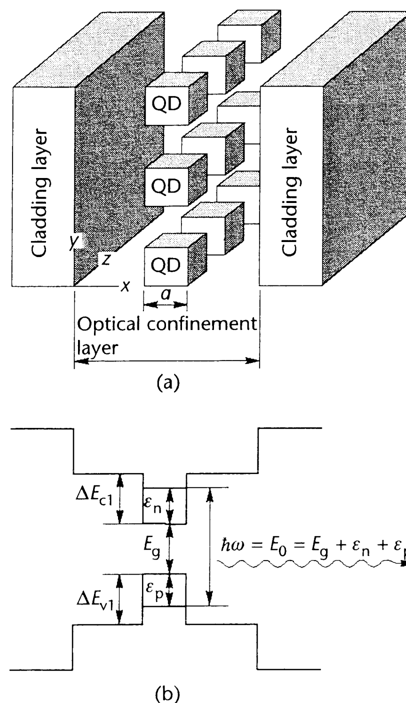

Figure 4.2 (a) Schematic structure and (b) energy band diagram of a QD laser.

4.4.1 Nonuniformity of QDs

Nonuniformity is a problem of great concern. As discussed earlier, the advantages of QD lasers stem from a δ-function-like density of states. If all QDs were identical, the gain spectrum would also be a δ function (Figure 4.1). However, the QDs in actual structures vary, primarily in size (Figure 4.3) and shape, but also in the local strain. The QD parameter dispersion causes fluctuations in the quantized energy levels. This leads to an inhomogeneous broadening in the optical transition energy (Figure 4.3) and hence also broadens the gain spectrum. This dispersion is hardly avoidable during the QD structures' growth: Size fluctuations are inherent in self-organized QD ensembles either fabricated by MBE or MOCVD.

Inhomogeneous line broadening is the key factor degrading the characteristics of a QD laser [30]. The QD parameter dispersion adversely affects the operating characteristics of a laser:

- Maximum gain decreases.
- Threshold current increases and becomes more sensitive to temperature (the characteristic temperature decreases).
- The multimode generation threshold decreases.
- The internal differential efficiency and output power both decrease.

The QD laser advantages can only be realized if the QDs are sufficiently uniform. Later we discuss how the threshold and power characteristics of a laser depend on the QD size fluctuations, that is, on the "degree" of the structure perfection.

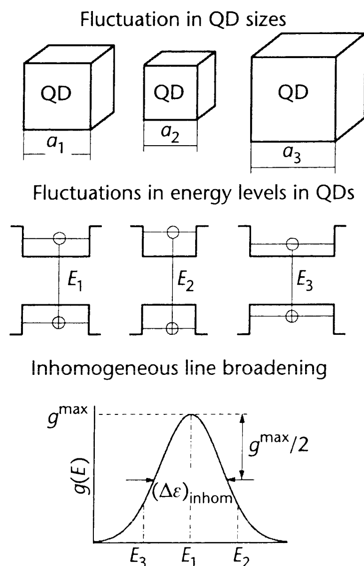

Figure 4.3 Inhomogeneous line broadening arising from nonuniformity of QDs.

Effect on the Gain

The laser threshold condition is

$$g^{\mathrm{m}} = \beta \tag{4.1}$$

where g^{m} is the peak value of the modal gain spectrum and β is the total loss. The minimum injection current satisfying (4.1) is, by definition, the threshold current.

The shape of the modal gain spectrum (which represents the effective gain of the active layer comprising QDs) and its transformation with the injection current are quite different in the two limits, corresponding to small and large QD size dispersions [30–32].

For small fluctuations (the inhomogeneous line broadening is less than the temperature T), the gain spectrum copies the curve for the QD size distribution, with the scale along the vertical axis determined by the population inversion in the QD of average size [Figure 4.4(a)]. The spectrum changes self-similarly with the current.

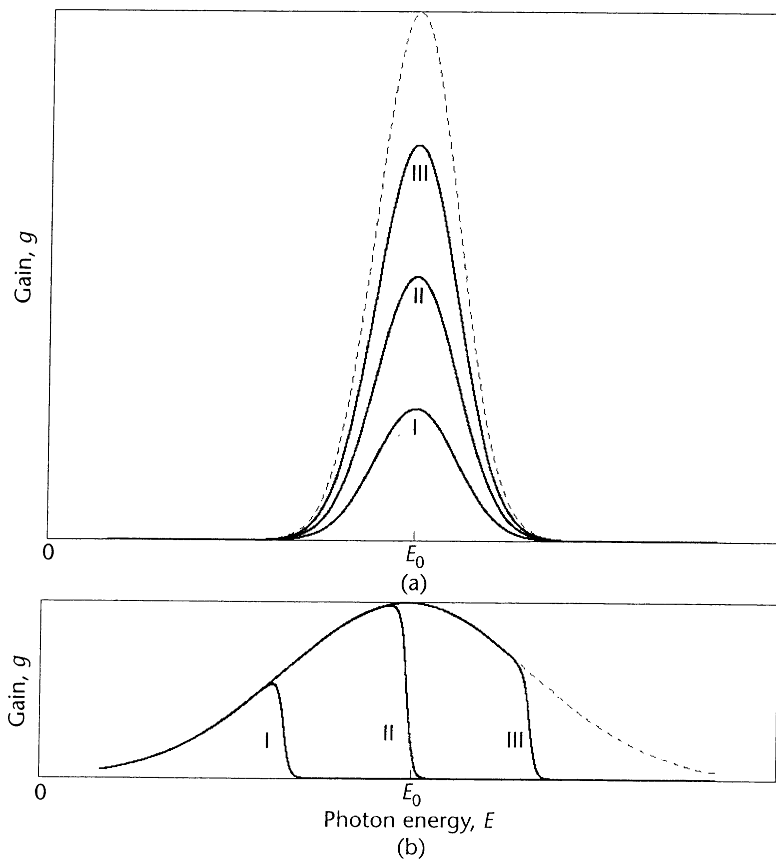

Figure 4.4 Gain spectra for equilibrium filling of quantum dots: (a) small dispersion, (b) large dispersion. Curves are numbered in order of increasing population inversion in a QD. The dashed curves correspond to full population inversion. (*From:* [30]. © 1996 IEEE. Reprinted with permission.)

The peak value of the modal gain spectrum occurs at the transition energy E_0 in a mean-sized QD and is equal to

$$g^{\mathrm{m}} = g^{\max}\left(f_n + f_p - 1\right) \tag{4.2}$$

where f_n and f_p are the occupancies of the quantized energy levels of an electron and a hole in a mean-sized QD.

The quantity $g^{\max}$ is the maximum possible (saturation) value of g^{m}. It holds when both f_n and f_p approach unity, that is, when the QDs are fully occupied. The dependence of $g^{\max}$ on the inhomogeneous line broadening $(\Delta\varepsilon)_{\mathrm{inhom}}$ is given by the following expression:

$$g^{\max} = \frac{\xi}{4}\left(\frac{\lambda_0}{\sqrt{\varepsilon}}\right)^2 \frac{1}{\tau_{\mathrm{QD}}} \frac{\hbar}{(\Delta\varepsilon)_{\mathrm{inhom}}} \frac{1}{\mathfrak{L}} N_S \tag{4.3}$$

where $\xi = 1/\pi$ and $\xi = 1/\sqrt{2\pi}$ for the Lorentzian and Gaussian distributions, respectively. $\lambda_0 = 2\pi\hbar c/E_0$ is the lasing wavelength; ε is the dielectric constant of the *optical confinement layer* (OCL); $\mathfrak{L}$ is the characteristic length of the optical confinement in the transverse waveguide direction; and N_S is the surface density of QDs.

The reciprocal spontaneous radiative recombination time for transitions between the quantized energy levels in the conduction and the valence bands is of the form

$$\frac{1}{\tau_{\mathrm{QD}}} = \frac{8}{3}\alpha\sqrt{\varepsilon}\,\frac{E_0}{\hbar}\left(\frac{P}{\hbar c}\right)^2 I \tag{4.4}$$

where $\alpha = e^2/\hbar c$ is the fine structure constant, P is Kane's parameter [33], and I is the overlap integral between the electron and hole wave functions (see Section 4.4.8).

The inhomogeneous line broadening caused by fluctuations in QD sizes is

$$(\Delta\varepsilon)_{\mathrm{inhom}} = \left(q_n\varepsilon_n + q_p\varepsilon_p\right)\delta \tag{4.5}$$

where $q_{n,p} = -\partial \ln\varepsilon_{n,p}/\partial \ln a$, $\varepsilon_{n,p}$ are the quantized energy levels in a mean-sized QD, a is the mean size of QDs, and δ is the *root mean square* (rms) of relative QD size fluctuations.

The gain saturation effect is observed experimentally in QD lasers. Because $g^{\max} \propto 1/(\Delta\varepsilon)_{\mathrm{inhom}}$, we see how crucial the QD size uniformity is.

For large fluctuations [$(\Delta\varepsilon)_{\mathrm{inhom}} > T$], the gain spectrum gradually fills the curve for the QD size distribution with increasing injection current [Figure 4.4(b)]. Both self-similar and gradually filled gain spectra have been observed experimentally.

Effect on the Threshold Current

Below and at the lasing threshold, the injection current density is consumed by the spontaneous recombination in QDs and in the OCL:

$$j = \frac{eN_S}{\tau_{\mathrm{QD}}} \langle f_n f_p \rangle + ebBnp \tag{4.6}$$

where $\langle \ldots \rangle$ means averaging over the QD ensemble, b is the thickness of the OCL, B is the radiative constant for the OCL, and n and p are the free-carrier densities in the OCL.

If we consider relatively high temperatures, the carriers in each band are close to equilibrium and in steady state the free-carrier densities in the OCL (below and at the threshold) can be expressed in terms of the confined-carrier level occupancies in a mean-sized QD [30]:

$$n = n_1 \frac{f_n}{1 - f_n}, \; p = p_1 \frac{f_p}{1 - f_p} \tag{4.7}$$

Here the quantities n_1 and p_1 are

$$n_1 - N_c \exp\left(- \frac{\Delta E_{c1} - \varepsilon_n}{T} \right), \; p_1 = N_v \exp\left(- \frac{\Delta E_{v1} - \varepsilon_p}{T} \right) \tag{4.8}$$

where $N_{c,v}$ are the conduction and valence band effective densities of states and $\Delta E_{c1,\,v1}$ are the band offsets at the QD–OCL heterointerface (Figure 4.2).

Assuming charge neutrality in QDs, $f_n = f_p$ (which is not the general case—see Section 4.3), (4.1) and (4.2) yield the level occupancies at threshold in a mean-sized QD:

$$f_{n,p} = \frac{1}{2}\left(1 + \frac{\delta}{\delta^{\max}} \right) \tag{4.9}$$

where $\delta^{\max}$ is the maximum tolerable rms of relative QD size fluctuations [see (4.43) in Section 4.4.7].

With (4.9), (4.7) and (4.6) yield the dependence on δ of both the free-carrier densities in the OCL at the lasing threshold and the threshold current density:

$$n_{\mathrm{th}} = n_1 \frac{1 + \frac{\delta}{\delta^{\max}}}{1 - \frac{\delta}{\delta^{\max}}}, \; p_{\mathrm{th}} = p_1 \frac{1 + \frac{\delta}{\delta^{\max}}}{1 - \frac{\delta}{\delta^{\max}}} \tag{4.10}$$

$$j_{\mathrm{th}} = \frac{1}{4} \frac{eN_S}{\tau_{\mathrm{QD}}} \left(1 + \frac{\delta}{\delta^{\max}} \right)^2 + ebBn_1 p_1 \frac{\left(1 + \frac{\delta}{\delta^{\max}} \right)^2}{\left(1 - \frac{\delta}{\delta^{\max}} \right)^2} \tag{4.11}$$

We see that the threshold current diverges as the dispersion increases and approaches a certain critical value, $j_{th} \to \infty$ for $\delta \to \delta^{max}$ [Figure 4.5(b)]. Such behavior has been observed experimentally [34].

In the opposite limit, j_{th} decreases and as $\delta \to 0$, the threshold current tends to the transparency (inversion) value, corresponding to the current density, at which $f_n + f_p - 1 = 0$ [Figure 4.5(b)].

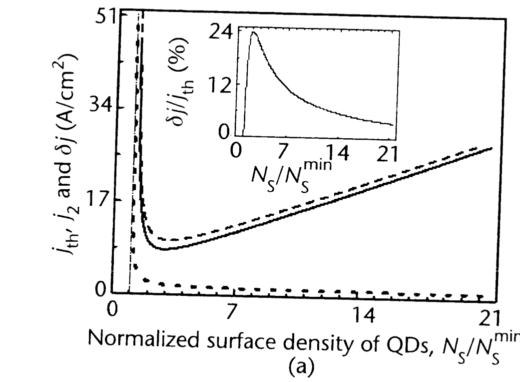

(a)

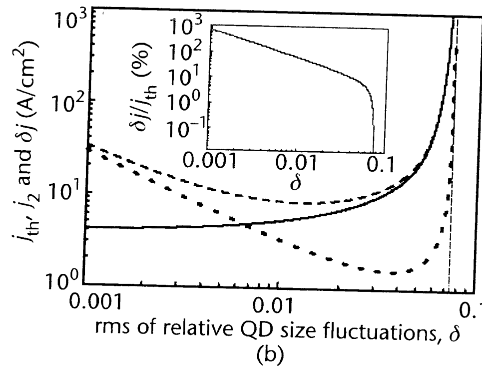

(b)

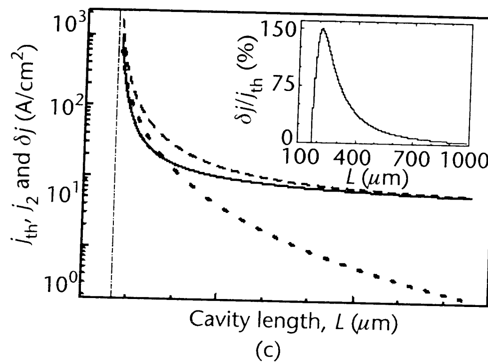

(c)

Figure 4.5 Multimode generation in a QD laser as function of (a) normalized surface density of QDs, (b) rms of relative QD size fluctuations, and (c) cavity length. Solid and dashed curves describe the threshold current density for the main mode and the next longitudinal mode, respectively, while dotted curves correspond to the multimode generation threshold. The insets show the relative multimode generation threshold. (*From:* [37]. © 2000 IEEE. Reprinted with permission.)

Effect on the Temperature Dependence of Threshold Current

The T dependence of j_{th} is described by the characteristic temperature T_0 [defined by (4.17)]. The higher this parameter, the less sensitive j_{th} is to temperature. Nonuniformity of QDs has a twofold effect on the T dependence of j_{th}. The main effect is through the thermal population of the OCL, which controls the parasitic recombination current outside QDs [30–32, 35]. The second effect is through the thermal population of nonlasing QDs, which gives rise to a parasitic recombination current [36].

Effect Through the Parasitic Recombination Outside QDs

The OCL is a nonlasing 3D region surrounding QDs. The carrier population in the OCL is in approximate thermal equilibrium with that in QDs, except at low temperatures. The recombination current in the OCL is the main source of temperature dependence of j_{th} (see later sections). Assuming charge neutrality in QDs, the following expression is obtained for T_0 as a function of δ [35]:

$$T_{0,\text{ neutral}} = \left[1+\frac{\frac{1}{4}\frac{N_S}{\tau_{QD}}\left(1-\frac{\delta}{\delta^{\max}}\right)^2}{bBn_1 p_1}\right]\frac{1}{\frac{3}{2}\frac{1}{T}\frac{\Delta E_{g1}-\varepsilon_n-\varepsilon_p}{T^2}} \tag{4.12}$$

where $\Delta E_{g1} = \Delta E_{c1} + \Delta E_{v1}$ is the bandgap difference between the materials of the OCL and QD.

The more uniform the QD ensemble, the lower the carrier density [see (4.8) and (4.10)] and the recombination current [the second term on the right side of (4.11)] in the OCL and the higher the T_0 (Figure 4.6). At room temperature and $N_S = 1.3 \times 10^{11}$ cm^{-2}, $\beta = 10$ cm^{-1} and 10% QD size dispersion ($\delta = 0.05$), the characteristic temperature for the structure optimized to minimize the threshold current density [30] is T_0

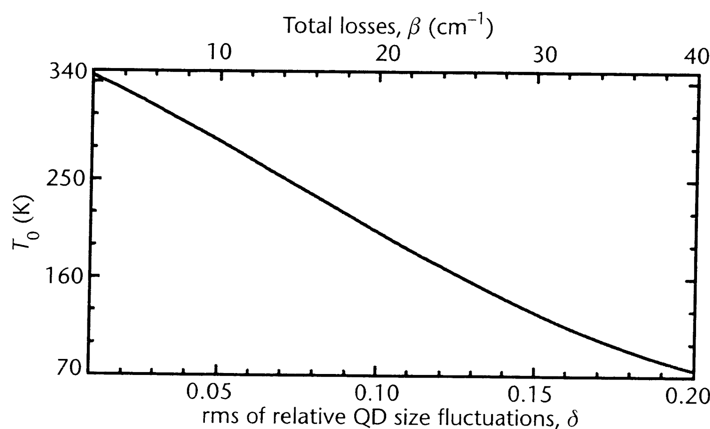

Figure 4.6 Characteristic temperature against rms of relative QD size fluctuations (at $\beta = 10$ cm^{-1}, bottom axis) and against total losses (at $\delta = 0.05$, top axis). $N_S = 1.3\times10^{11}$ cm^{-2}. (*From:* [35]. © 1998 IEEE. Reprinted with permission.)

≈ 286K [35]. This estimate is several times higher than the best T_0 in QW lasers for the same loss (typically less than 90K).

Effect Through the Recombination in Nonlasing QDs

Because of the inhomogeneous broadening, a certain fraction of QDs does not contribute to the lasing transitions while still adding to the parasitic recombination. As far as T_0 is concerned, the effect of thermal population of nonlasing QDs is in principle similar to (but not as strong as) that due to carriers residing in the OCL.

The thermal population of nonlasing QDs and hence the T dependence of the recombination current in QDs, j_{QD} [the first term on the right side of (4.6)], is simply accounted for by the deviation of $\langle f_n f_p \rangle$ from the product of the electron and hole level occupancies in a mean-sized QD. The characteristic temperature for j_{QD} is [36]

$$\frac{T_{0,\,\mathrm{inhom}}^{\mathrm{QD}}}{T}=\frac{1-\dfrac{a^2\delta^2}{2}(1-f_n)\left[\dfrac{\varepsilon''_n+\varepsilon''_p}{T}-\dfrac{\varepsilon'_n}{T}\dfrac{\varepsilon'_p}{T}(1-f_n)+\dfrac{{\varepsilon'_n}^2+{\varepsilon'_p}^2}{T^2}(2f_n-1)\right]}{\dfrac{a^2\delta^2}{2}(1-f_n)\left[\dfrac{\varepsilon''_n+\varepsilon''_p}{T}-2\dfrac{\varepsilon'_n}{T}\dfrac{\varepsilon'_p}{T}(1-f_n)+2\dfrac{{\varepsilon'_n}^2+{\varepsilon'_p}^2}{T^2}(2f_n-1)\right]} \tag{4.13}$$

where f_n is the level occupancy in a mean-sized QD at the lasing threshold given by (4.9), and $\varepsilon'_{n,p}$ and $\varepsilon''_{n,p}$ are, respectively, the first and the second derivatives of $\varepsilon_{n,p}$ with respect to the QD size taken at the mean size of the QD's a.

The dependence of $T_{0,\mathrm{inhom}}^{\mathrm{QD}}$ on δ is nonmonotonic (Figure 4.7). The decrease of $T_{0,\mathrm{inhom}}^{\mathrm{QD}}$ at small δ is due to the increasing thermal population of nonlasing QDs. At large QD size dispersion, when $\delta \to \delta^{\max}$, f_n approaches unity [see (4.9)] to satisfy the

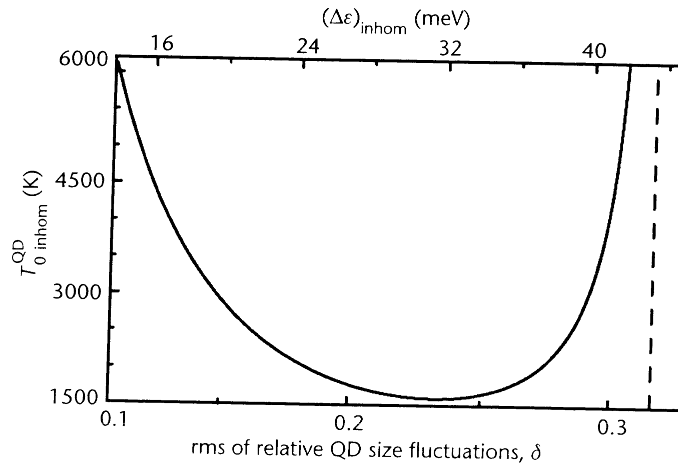

Figure 4.7 Characteristic temperature $T_{0,\mathrm{inhom}}^{\mathrm{QD}}$ as a function of the rms of relative QD size fluctuations (bottom axis) and the inhomogeneous line broadening (top axis). The vertical dashed line indicates $\delta^{\max}$. (*From:* [36]. © 2001 IEEE. Reprinted with permission.)

threshold condition; full occupancy of QDs forces temperature independence of j_{QD} at the expense of a very large increase in the total threshold current.

The characteristic temperature $T_{0,\text{inhom}}^{QD}$ is much higher than $T_{0,\text{neutral}}$ given by (4.12): As seen from Figure 4.7, $T_{0,\text{inhom}}^{QD}$ is above 1,500K over the entire range of δ. Such a characteristic temperature can be essentially considered infinite for most practical purposes. Hence, the effect of thermal population of nonlasing QDs is negligible compared to that of the nonlasing 3D region surrounding QDs.

Effect on the Multimode Generation Threshold

The multimode behavior of lasing in QD structures is caused by spatial hole burning (Section 4.4.5) [37].

The multimode generation threshold δj is defined as the excess of the injection current density over the threshold current density for the main mode, at which the lasing oscillation of the next (closest to the main) mode of the resonator begins. The following equation is obtained for δj as a function of δ at relatively high T [37]:

$$\delta j = 2\left[\frac{\hbar \frac{c}{\sqrt{\varepsilon}} \frac{\pi}{L}}{\left(q_n \varepsilon_n + q_p \varepsilon_p\right)\delta}\right]^2 \frac{\delta}{\delta^{\max}} \frac{1}{1-\frac{\delta}{\delta^{\max}}} \frac{eN_S}{\tau_n^{\text{esc}} + \tau_p^{\text{esc}}} \tag{4.14}$$

where L is the cavity length and $\tau_{n,p}^{\text{esc}}$ are the thermal escape times of electrons and holes from QDs. These times are given by

$$\tau_n^{\text{esc}} = \frac{1}{\sigma_n v_n n_1}, \tau_p^{\text{esc}} = \frac{1}{\sigma_p v_p p_1} \tag{4.15}$$

where $\sigma_{n,p}$ are the QD capture cross sections and $v_{n,p}$ are thermal velocities.

We see that decreasing the QD size dispersion improves the single-mode behavior of the laser, in addition to the improvements in threshold current and temperature stability. As $\delta \to 0$, the multimode generation threshold increases indefinitely, diverging as δ^{-1} [Figure 4.5(b)].

Effect on the Internal Quantum Efficiency and the Output Power

We have discussed the effect of QD size dispersion on threshold characteristics. The QD uniformity is of crucial importance also for the high-power characteristics of a laser [38, 39].

The general expression for the internal quantum efficiency η_{int} of quantum confined lasers is (4.31) in a later section. As δ approaches its maximum tolerable value $\delta^{\max}$ [given by (4.43)], the internal quantum efficiency and the output power both vanish (Figure 4.8). The more uniform the QD ensemble, the higher η_{int} (Figure 4.8), the more linear the *light-current characteristic* (LCC) and the higher the output power (Figures 4.8 and 4.9). In properly optimized QD lasers, discussed later, the

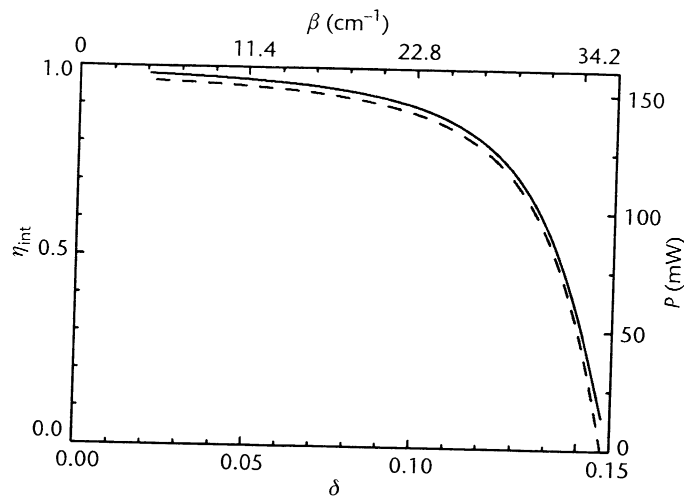

Figure 4.8 Internal quantum efficiency (solid curve, left axis) and output power (dashed curve, right axis) as a function of the rms of relative QD size fluctuations (at fixed $L = 1$ mm, bottom axis) and the cavity loss (at fixed $\delta = 0.05$, top axis). (*From:* [39]. © 2003 IEEE. Reprinted with permission.)

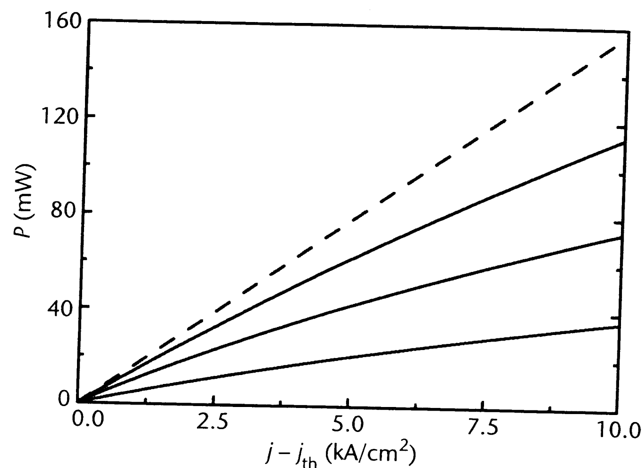

Figure 4.9 LCC for structures with different rms of relative QD size fluctuation. The dashed line corresponds to the ideal situation, $\eta_{int} = 1$. The values of δ and j_{th} (from the top down) are, respectively, 0.13, 0.145, 0.153, 122.44, 465.32, and 1,937 A/cm^2. (*From:* [39]. © 2003 IEEE. Reprinted with permission.)

LCC can be linear and η_{int} can be close to unity up to very high current densities (15 kA/cm^2); output powers in excess of 10W at η_{int} higher than 95% are attainable in broad-area devices. These results indicate that QD lasers may possess an advantage over conventional QW lasers for high-power applications.

4.4.2 Parasitic Recombination Outside QDs

In "traditional" QD laser structures, the QDs are surrounded by the OCL, which itself is conductive and transports mobile carriers to the QDs. (This situation is common to all semiconductor diode lasers.) Carriers are first injected from the cladding layers to the OCL and then captured into QDs. A two-step supply of carriers into the active region, wherein stimulated transitions occur, is detrimental to both the threshold and high-power characteristics. As a result of such an indirect, OCL-mediated injection into the active region, (1) the threshold current and its temperature-sensitivity both increase and (2) the internal quantum efficiency and the output power decrease. A new approach to the QD laser design, which eliminates the troublesome recombination outside the active region, is discussed in Section 4.4.5.

Effect on the Threshold Current

High temperature stability of operation is an essential feature required of long-wavelength diode lasers for telecommunications. Commercial QW lasers based on InGaAsP/InP heterosystem are rather poor in this respect; the characteristic temperature T_0 reaches, at best, about 90K.

Ideally, threshold current of a QD laser should remain unchanged with the temperature, that is, T_0 should be infinitely high [8]. This would be so indeed if the overall injection current went entirely into the radiative recombination in QDs. However, a fraction of the current occurs by recombination in the OCL. This component of j_{th}, denoted as j_{OCL} [the second term on the right side of (4.11)], is associated with thermal excitation of carriers from QDs and hence depends exponentially on T [30, 35]. It is this component that is mainly responsible for the T dependence of j_{th} at room temperature and above. Such a mechanism of T dependence is also at play in other semiconductor lasers, but in QD lasers it plays the central role. Inasmuch as the growth technology allows us to fabricate reasonably uniform QD arrays, so that the inhomogeneous line broadening is controlled to a high degree, it is the thermal exchange between the QDs and the OCL that remains the main obstacle to full realization of the advantages of 3D confinement.

Assuming charge neutrality, the T dependence of j_{OCM} (Figure 4.10) is apparent from (4.11) and (4.8):

$$j_{\mathrm{OCL,\,neutral}}(T) \propto Bn_1 p_1 \propto T^{3/2} \exp\left(-\frac{\Delta E_{\mathrm{g1}} - \varepsilon_{\mathrm{n}} - \varepsilon_{\mathrm{p}}}{T}\right) \tag{4.16}$$

(Temperature dependences of the radiative constant B [30] and of the conduction and valence band effective densities of states $N_{c,v}$ have also been taken into account here.)

With the increasing energy $\Delta E_{g1} - \varepsilon_n - \varepsilon_p = (\Delta E_{c1} - \varepsilon_n) + (\Delta E_{v1} - \varepsilon_p)$, which is the sum of the localization energies of electrons and holes in a mean-sized QD, the free-carrier densities in the OCL decrease and hence so does j_{OCL}. This makes j_{th} less sensitive to temperature. In [40], the OCL was made of AlGaAs, which has a wider

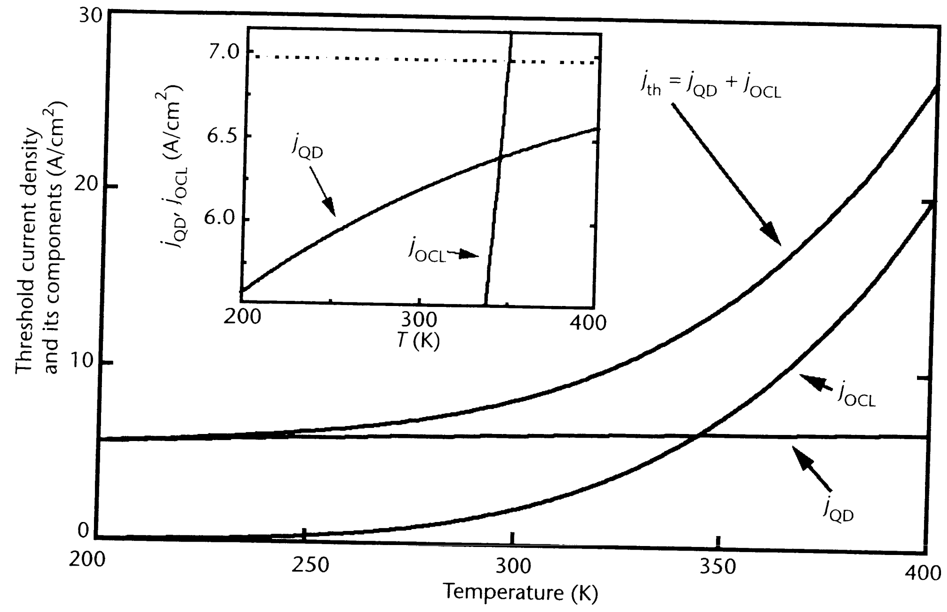

Figure 4.10 Temperature dependence of the threshold current density and its components. The inset shows $j_{QD}(T)$ and $j_{QCL}(T)$ on an enlarged (along the vertical axis) scale. The dashed line shows j_{QD} calculated assuming the charge neutrality in QDs. (*From:* [35]. © 2003 IEEE. Reprinted with permission.)

bandgap than GaAs, in order to suppress the thermal escape of carriers from QDs. This led to a significant reduction of j_{th}.

Effect on the Characteristic Temperature T_0

The characteristic temperature is the key parameter describing empirically the T dependence of the threshold current of semiconductor lasers. It is defined as follows [41]:

$$T_0 = \left(\frac{\partial \ln j_{th}}{\partial T} \right)^{-1} \tag{4.17}$$

Although $j_{th}(T)$ never fits the exponential form $\exp(T/T_0)$ precisely [as might appear from (4.17)], it is usually adequately characterized by the parameter T_0 within a narrow temperature range of interest. Considering a wider range, T_0 itself is a function of the temperature.

The dependence $T_0 = T_0(T)$ is strong [21] and shows a deep fall-off with increasing temperature (Figure 4.11). The drastic decrease in T_0 is explained [35] by the transition from the low-T regime, when j_{th} is controlled by recombination in QDs, to the regime at higher T, when j_{th} is controlled by the parasitic recombination in the OCL.

At relatively high T, charge neutrality violation has negligible effect on the T dependence of j_{th} (Figure 4.11) and T_0 is approximately given by (4.12). The factor outside the square brackets in (4.12) corresponds to a characteristic temperature $T_{0,\text{inhom}}^{\text{QD}}$ defined for the function $j_{\text{OCL, neutral}}(T)$ given by (4.16).

As discussed in an earlier section, the nonuniformity of QDs affects the threshold current and its temperature stability primarily through the parasitic recombination outside QDs. Equation (4.9) shows that when δ approaches its maximum tolerable value $\delta^{\max}$, the level occupancies in QDs tend to unity. Full occupancy of QDs requires infinitely high free-carrier densities in the OCL [see (4.10)]. Hence the recombination current density on the OCL [the second term on the right side of (4.11)] also increases infinitely.

Effect on the Internal Quantum Efficiency and the Output Power

Power characteristics are also strongly affected by the recombination outside QDs. As discussed later in Section 4.4.6, due to the noninstantaneous nature of carrier capture into QDs, the carrier density and the recombination current in the OCL both continue increasing with the injection current above the lasing threshold. This causes a deviation of the internal efficiency η_{int} from unity. Furthermore, since the recombination rate in the OCL is superlinear in the carrier density (first quadratic and then cubic), the internal efficiency becomes a decreasing function of the injection current, and hence the LCC is sublinear [38, 39].

It is the ratio of the threshold values of the parasitic recombination current outside QDs to the capture current into QDs that determines η_{int} and the output power

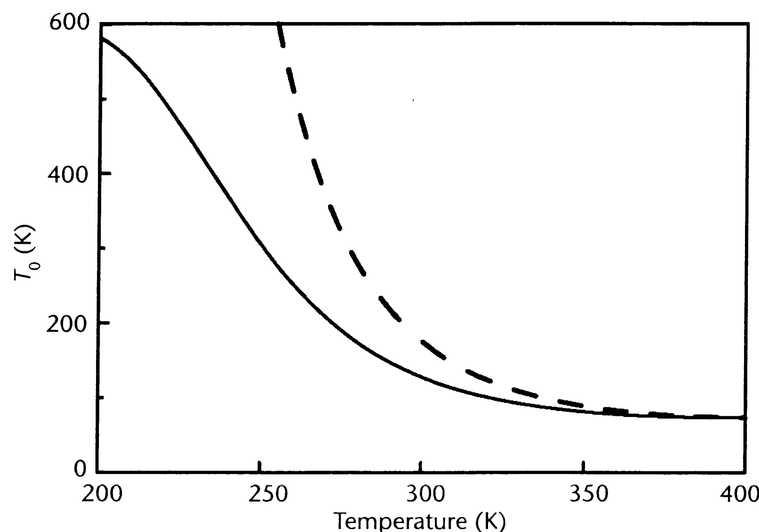

Figure 4.11 Temperature dependence of the characteristic temperature. The dashed curve shows T_0 calculated assuming charge neutrality in QDs [see (4.12)]. (*From:* [35]. © 1998 IEEE. Reprinted with permission.)

at a given injection current [38, 39]. Figure 4.12 shows how important the lowering of this ratio is to enhance η_{int} and the output power. We discuss this issue in greater detail in a later section.

4.4.3 Violation of Local Neutrality in QDs

As shown in [42], the electron level occupancy in a QD may differ from that of a hole; that is, QDs may be charged. The QD structures are distinct in this sense from similar QW structures in that the difference between the hole and the electron level occupancies in a QD, $f_p - f_n$, can be comparable to the occupancies, f_n and f_p, themselves (see [42] and Figure 4.13). The distinction is rooted in the low surface density of QDs, N_S (typically from several 10^{10} cm^{-2} to 10^{11}cm^{-2}), compared to the 2D-carrier density in a QW (typically above 10^{12}cm^{-2}). The same amount of surface charge density, $eN_S (f_p - f_n)$, required to screen a local electric field inhomogeneity, gives a tangible charge imbalance in the layer of QDs, while being quite negligible relative to the overall electron or hole charge in a QW. This is the reason why QWs can be considered neutral [43, 44] and QDs, in general, cannot.

The violation of local neutrality in QDs strongly affects the threshold characteristics of a laser. In the absence of neutrality, (4.1) alone does not determine the electron and hole level occupancies in a QD at the lasing threshold. One needs an additional relation between f_n and f_p. This relation can be obtained by solving a self-consistent problem for the electrostatic field distribution across the heterojunction. Generally, it can be written in the form:

$$f_p - f_n = \Delta \tag{4.18}$$

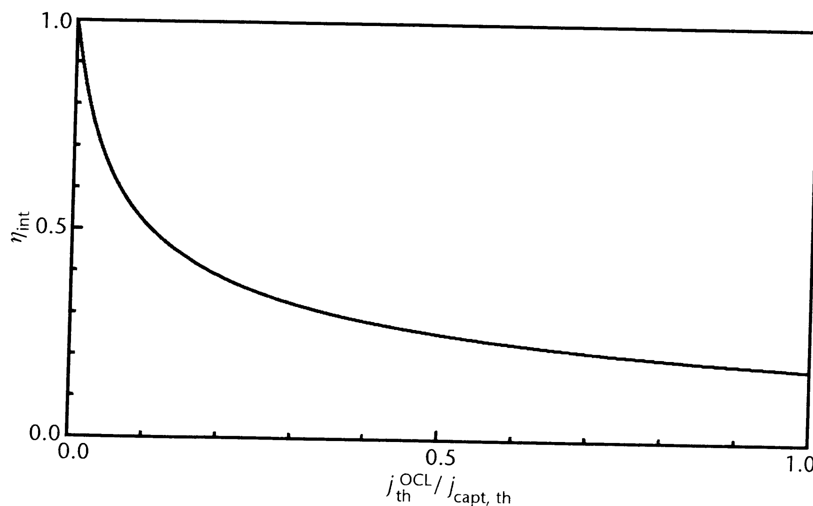

Figure 4.12 Internal quantum efficiency as a function of the ratio $j_{th}^{OCL}/j_{capt,\,th}$. Injection current density $j = 10$ kA/cm^2; the variation of $j_{th}^{OCL}/j_{capt,\,th}$ in the range shown (from 8×10^{-4} to 1) is accomplished by changing N_S from 20 × to 2.81×10^{10} cm^{-2}. (*From:* [39]. © 2003 IEEE. Reprinted with permission.)

A specific type of the function Δ depends on details of the laser structure, for example, on the spatial distribution of donor and acceptor impurities and the band offsets.

With (4.18), the level occupancies in a mean-sized QD at the lasing threshold are:

$$f_n = \frac{1}{2}\left(1 + \frac{\delta}{\delta^{\max}} - \Delta\right), f_p = \frac{1}{2}\left(1 + \frac{\delta}{\delta^{\max}} + \Delta\right) \tag{4.19}$$

When the local neutrality holds (Δ = 0), the threshold level occupancy is temperature insensitive [see (4.9)]. Due to the T dependence of Δ, the violation of charge neutrality is accompanied by a T dependence of f_n and f_p (Figure 4.13). Unconstrained by the neutrality condition, f_n and f_p are no longer fixed by the threshold condition and become T dependent. As a result, the threshold current density component j_{QD} associated with the radiative recombination in QDs is also T dependent (Figure 4.10). Thus, even if the parasitic recombination outside QDs is fully suppressed, there remains a T dependence of j_{th}, associated with the violation of QD neutrality. It is this effect that keeps finite the characteristic temperature T_0 (Figure 4.11) at low T (as already observed in the first QD laser [21], when the thermal escape of carriers from QDs is essentially suppressed.

The equation for $T_{0,\mathrm{VCN}}^{\mathrm{QD}}$ defined for $j_{QD}(T)$ is

$$\frac{1}{T_{0,\mathrm{VCN}}^{\mathrm{QD}}} = \frac{1}{4}\frac{1}{f_n f_p}\frac{\partial \Delta^2}{\partial T} \tag{4.20}$$

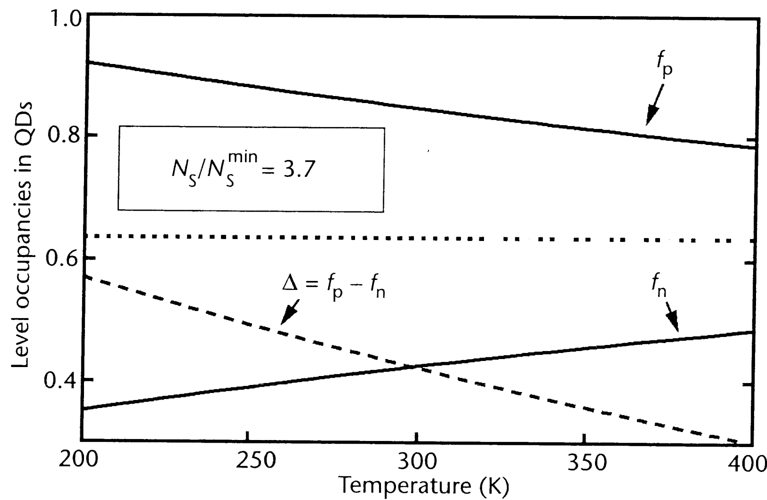

Figure 4.13 Temperature dependence of the electron and hole level occupancies and their difference at the lasing threshold. The horizontal dotted line shows $f_{n,p}$ calculated assuming charge neutrality in QDs. $\beta = 10\ \mathrm{cm}^{-1}$ and $\delta = 0.05$; $N_S^{min} = 2.1 \times 10^{10}\ \mathrm{cm}^{-2}$. (*From:* [35]. © 1998 IEEE. Reprinted with permission.)

The obtained characteristic temperature $T_{0,\text{VCN}}^{\text{QD}}$ is positive because the absolute value of Δ always decreases with T (Figure 4.13).

At relatively low T, when j_{th} is controlled by j_{QD}, the values of $T_{0,\text{ neutral}}$ obtained from (4.12) (Figure 4.11, dashed curve) are far larger than the actual T_0 calculated taking into account violation of neutrality (Figure 4.11, solid curve).

4.4.4 Excited States

Ideally, there should be one electron and one hole energy level in a QD, since the presence of excited carrier states may degrade some of the advantages of QD lasers. This complication would not be as severe for highly symmetrical (e.g., cubic) QDs, where multiple hole levels can be tolerated provided one has only one electron level. The reason is that radiative transitions from the ground electron state to excited hole states are forbidden by the selection rules in sufficiently symmetrical structures. However, such transitions are allowed in actual, low-symmetry (e.g., pyramidal) QDs. Moreover, there may also be excited electron states [45].

In the context of lowering j_{th} and enhancing T_0 excited state transitions are undesirable. On the other hand, from the standpoint of increasing the maximum gain, their presence may even be beneficial. It is via such transitions that lasing often occurs in short-cavity QD structures. Interestingly, the observed switch of the lasing wavelength with the cavity length (see, e.g., [46]) can be attributed to the contribution of these "forbidden" transitions [47, 48].

A detailed theoretical study of the effect of excited state transitions on the threshold characteristics of a QD laser was given in [47, 48]. Here we discuss the effect of excited states on the T dependence of j_{th} [49].

The presence of excited states serves as another source of T dependence of j_{th}, because of the thermally activated parasitic recombination associated with excited state transitions. Denoting the characteristic temperature limited by the presence of excited states by T_0^{exc}, the ratio T_0^{exc}/T can be put in the form of a universal function of Δ^{exc}/T (where Δ^{exc} is the separation between the transition energies; see Figure 4.14):

$$\frac{T_0^{\text{exc}}}{\text{T}} = \frac{1}{1-r} \frac{\left[\left(\frac{1}{f_n}-1\right)\exp\left(\frac{\Delta^{\text{exc}}}{T}\right)+1\right]^3}{2\frac{\Delta^{\text{exc}}}{T}\left(\frac{1}{f_n}-1\right)\exp\left(\frac{\Delta^{\text{exc}}}{T}\right)} \left\{ r f_n^2 \frac{1-r}{\left[\left(\frac{1}{f_n}-1\right)\exp\left(\frac{\Delta^{\text{exc}}}{T}\right)+1\right]^2} \right\} \tag{4.21}$$

where f_n is the occupancy of the ground state in a mean-sized QD, $r = I_1/(I_1 + I_2)$, and I_1 and I_2 are the rates (the reciprocals of the spontaneous radiative lifetimes) of the ground and excited state transitions, respectively.

For small enough QDs, the T dependence of j_{th} arising from thermally excited states is negligible compared to the effects of parasitic recombination in the OCL and charge neutrality violation.

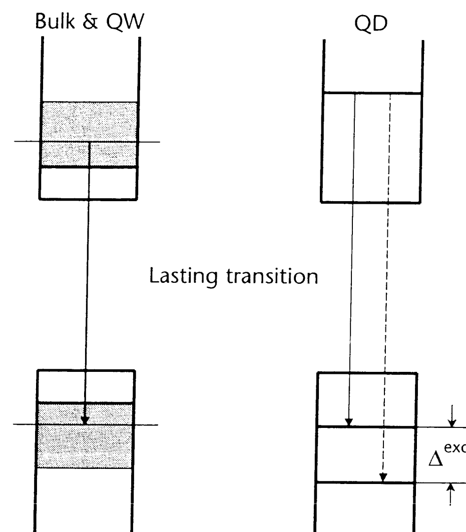

Figure 4.14 Carrier population in bulk, QW, and single QD. The dashed arrow shows the excited state transition in a QD. (*From:* [49]. © 2003 IEEE. Reprinted with permission.)

Suppression of the Effect of Excited States of Holes by *p*-Doping

In QDs supporting multiple closely spaced hole levels, the effect of excited states on the T sensitivity of j_{th} can be strong. Thermal smearing of the hole population among many states means that a large T-dependent fraction of injected holes is not in the ground state. Achieving the population inversion for lasing in such structures requires a T-dependent threshold current. To eliminate this problem, doping QDs with acceptors was proposed [26]. Owing to the larger separation of electron levels (due to the smaller effective mass), the injected electrons lie mostly in their ground state. The large hole occupancy built in by the p doping now ensures that injected electrons always find ground state holes to recombine. A high value of T_0 (160K) was achieved by this method [26].

4.4.5 Spatial Discreteness of Active Elements: Hole Burning

Spatial hole burning (SHB) in semiconductor [50, 51] and solid-state [52] lasers is due to the nonuniformity of stimulated recombination. It leads to the lasing oscillation of higher modes of the resonator together with the main mode. The problem of multimode generation is of primary importance for many laser applications [10]. To suppress the additional modes and properly design single-mode operating lasers, it is essential to understand the key physical processes controlling the multimode generation threshold.

In a QD laser, the SHB effect can be particularly strong in view of the spatial discreteness of QDs [37]. The point is that the stimulated emission in a laser cavity is a standing wave (with several thousands of wavelengths accommodated along the cavity length). The stimulated recombination will be most (least) intensive in the QDs located at the antinodes (nodes) of the light intensity (Figure 4.15). This gives

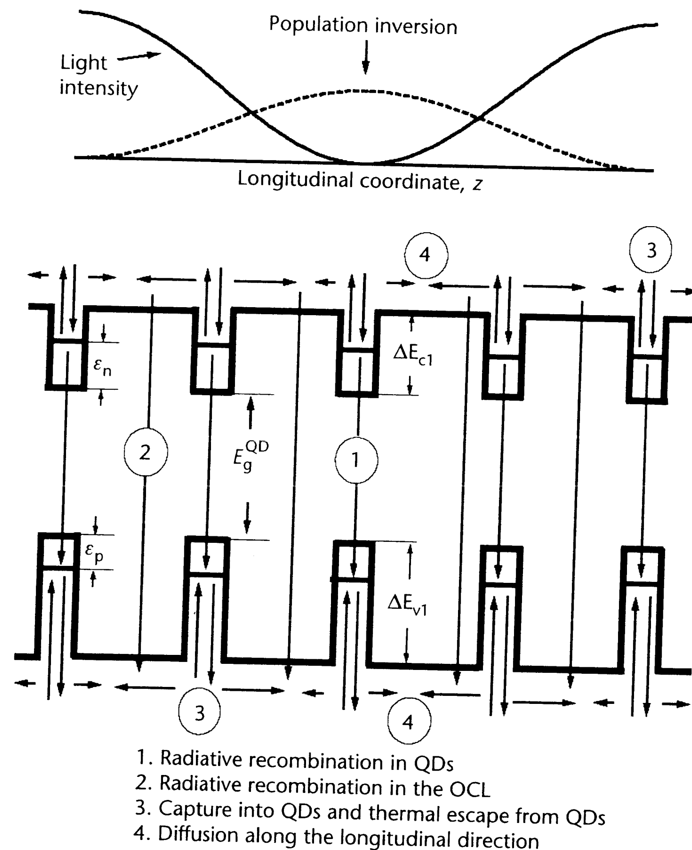

Figure 4.15 Schematic cross section of a QD laser structure along the longitudinal direction.

rise to SHB of the population inversion—QDs located near the antinodes (nodes) are depleted (overfilled).

In semiconductor bulk or QW lasers, the resultant nonuniform carrier distribution is smoothened out by diffusion, which partly or totally suppresses the SHB effect [50].

A drastically different situation occurs in QD lasers. Here, diffusion plays a minor role. Because only those carriers that are localized in the QDs contribute to the stimulated emission, the smoothing of nonuniform population inversion requires a series of transport processes: thermal escape of carriers from the overfilled QDs, diffusion in the OCL to the depleted QDs and capture into the latter (Figure 4.15). This slow carrier exchange between individual QDs may result in a highly nonuniform population inversion, and hence a strong SHB. This in turn implies that the multimode generation threshold may be low. A detailed study of SHB based on the steady-state rate equations (for confined carriers, free carriers, and photons) is presented in [37].

We can see from (4.14) that the multimode generation threshold δj is governed by the characteristic times $\tau_{n,p}^{esc}$ of the thermal escapes from QDs. Thermal escape,

rather than diffusion, is the slowest process controlling the smoothing of nonuniform population inversion. A similar situation arises in lasers based on band-to-impurity optical transitions [53, 54].

The temperature dependence of δj resides in the escape times $\tau_{n,p}^{esc}$ [see (4.8) and (4.15)]. The main reason is the exponential temperature dependence of the quantities n_1 and p_1. Concurrent with the unwelcome increase of j_{th}, the increasing T leads to a desirable increase of Δj (Figure 4.16). This occurs because the thermal escape from QDs becomes much more effective at high T. (Similarly, δj increases with T in semiconductor bulk lasers, due to the enhanced diffusion at higher T [50].) Thus, provided SHB is the only (or the main) factor that allows many modes to oscillate simultaneously, the number of the lasing modes decreases with increasing T and hence the LCC becomes more linear. This may explain the observed increase with T of the slope efficiency in a QD laser [55].

4.4.6 Intrinsic Nonlinearity of the Light-Current Characteristic

In every QW, QWR, or QD laser, the quantum-confined active elements are embedded in a bulk reservoir region, which also serves as the OCL, wherefrom carriers are fed via some sort of a capture process. Because the capture is never instantaneous, it gives rise to a current dependence of the carrier density n in the reservoir, even above threshold when the carrier density in the active region itself is pinned. The increasing

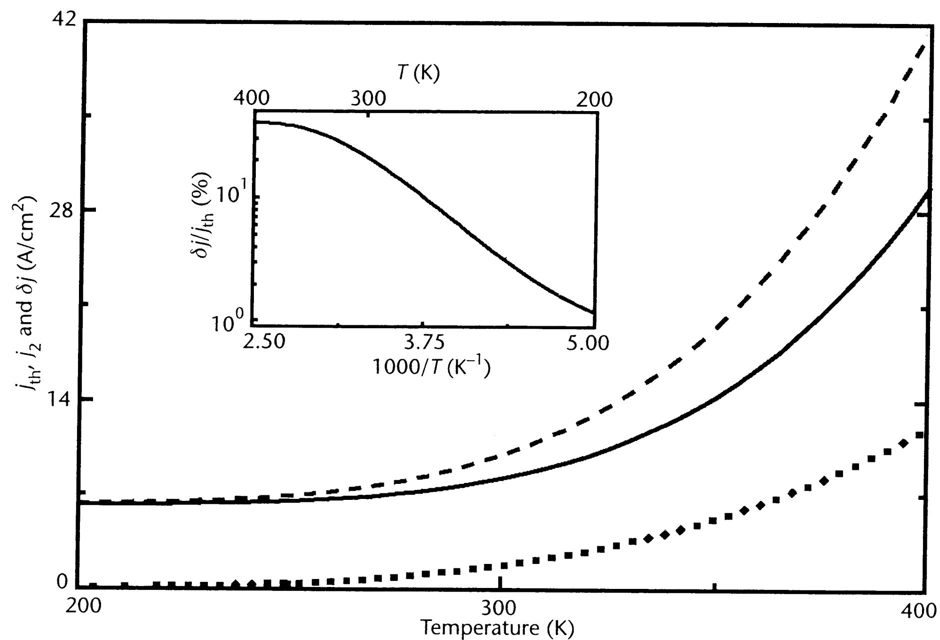

Figure 4.16 Temperature dependence of the multimode generation. Solid and dashed curves describe, respectively, the threshold current density for the main and the next longitudinal modes; the dotted curve corresponds to the multimode generation threshold. The relative multimode generation threshold is shown in the inset. (*From:* [37]. © 2000 IEEE. Reprinted with permission.)

n leads to an increase in the parasitic recombination current in the reservoir, and contributes to a deviation of the internal differential quantum efficiency η_{int} from unity. This fact was noted earlier [56–61] but the actual reduction in η_{int} was quantified only recently [38, 39].

The "reservoir effect," combined with the nonlinear (superlinear in n) dependence of the recombination rate in the reservoir, makes the *light-current characteristic* (LCC) sublinear at high injection currents [38, 39]. The resultant degradation of the LCC is comparable in magnitude to the entire experimentally observed degradation, even neglecting all other known mechanisms of nonlinearity (such as the lattice and carrier heating). This suggests that the reservoir effect is a dominant mechanism limiting both the output power and the linearity of the LCC.

Rate Equations

The steady-state rate equations for carriers confined in the active region, free carriers in the OCL and photons can be written as follows:

$$j_{capt} - j_{esc} - j_{spon}^{active} - j_{stim} = 0 \tag{4.22}$$

$$j_{esc} - j_{capt} - j^{OCL} + j = 0 \tag{4.23}$$

$$j_{stim} - e\frac{1}{S}\frac{N}{\tau_{ph}} = 0 \tag{4.24}$$

where j_{capt} and j_{esc} are, respectively, the current densities of carrier capture into and carrier escape from the active region, j_{spon}^{active} and j_{stim} are the spontaneous and the stimulated recombination current densities in the active region, j^{OCL} is the parasitic recombination current density in the OCL, j is the injection current density, S is the active layer area (the cross section of the junction), N is the number of photons in the lasing mode, and τ_{ph} is the photon lifetime in the cavity.

Taking into account that

$$j_{stim} - \frac{e}{S}\frac{c}{\sqrt{\varepsilon_g}} g^m N \tag{4.25}$$

where $\sqrt{\varepsilon_g}$ is the group refraction index of the OCL, it follows immediately from (4.24) that the modal gain spectrum peak g^m pins above threshold and hence so does the carrier density in the active region.

Because j_{esc} and j_{spon}^{active} are both controlled by the carrier density in the active region, they also clamp above threshold. On the other hand, the capture current is linear in the carrier density n in the OCL:

$$j_{capt} = ev_{capt}n = \frac{ebn}{\tau_{capt}} \tag{4.26}$$

where v_{capt} is the capture velocity (in centimeters per second) and τ_{capt} is the "capture time" into the active region. Thus, we obtain from (4.22)

$$n = n_{th}\left(1 + \frac{j_{stim}}{j_{capt,\,th}}\right) \tag{4.27}$$

where n_{th} and $j_{capt,\,th}$ are the threshold values of n and j_{capt}, respectively (n_{th} is not to be confused with the threshold carrier density in the active region). The slower the carrier supply to the active region (the lower $j_{capt,\,th}$), the larger is $n - n_{th}$.

Using (4.22) and (4.23) and taking into account that j_{spon}^{active} pins above threshold, the excess injection current density $j - j_{th}$ is

$$j - j_{th} = j^{OCL} - j_{th}^{OCL} + j_{stim} \tag{4.28}$$

where $j_{th} = j_{th}^{OCL} + j_{spon}^{active}$ is the threshold current density, with j_{th}^{OCL} being the value of j^{OCL} at $n = n_{th}$.

When the dominant recombination channel in the OCL is spontaneous radiation, then $j^{OCL} \propto n^2$ [with n given by (4.27)]. Using this in (4.28) yields

$$\frac{j - j_{th}}{j_{th}^{OCL}} = \left(1 + \frac{j_{stim}}{j_{capt,\,th}}\right)^2 - 1 + \frac{j_{stim}}{j_{th}^{OCL}} \tag{4.29}$$

Solution of quadratic equation (4.29) gives j_{stim} as a function of $j - j_{th}$; substituting this function into (4.27), we obtain an expression for n (Figure 4.17).

Direct Relationship Between the Power and the Threshold Characteristics

The internal differential quantum efficiency of a semiconductor laser is defined as the fraction of the excess injection current that results in stimulated emission:

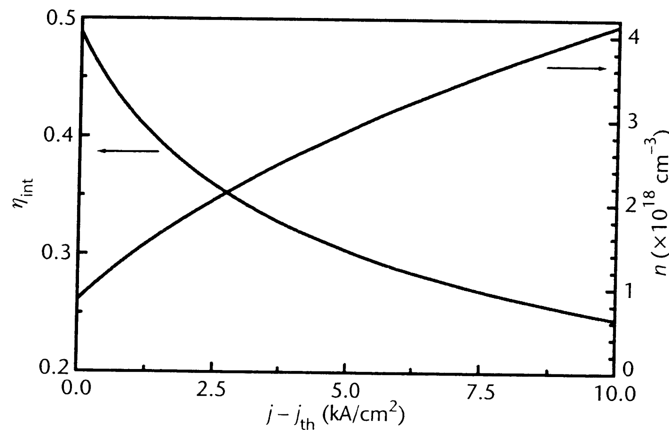

Figure 4.17 Internal quantum efficiency (left axis) and free-carrier density in the OCL (right axis) against excess injection current density, where j_{th} = 336.99 A/cm^2 and $j_{th}^{OCL} / j_{capt,\,th}$ = 0.523 at N_S = 2.9 × 10^{10} cm^{-2}. (*From:* [39]. © 2003 IEEE. Reprinted with permission.)

$$\eta_{\text{int}} = \frac{j_{\text{stim}}}{j - j_{\text{th}}} \tag{4.30}$$

Taking j_{stim} from (4.29), we find the following expression [38, 39]:

$$\eta_{\text{int}} = \frac{1}{\dfrac{1}{2} + \dfrac{j_{\text{th}}^{\text{OCL}}}{j_{\text{capt, th}}} + \sqrt{\left(\dfrac{1}{2} + \dfrac{j_{\text{th}}^{\text{OCL}}}{j_{\text{capt, th}}}\right)^2 + \dfrac{j_{\text{th}}^{\text{OCL}}}{j_{\text{capt, th}}} \dfrac{j + j_{\text{th}}}{j_{\text{capt, th}}}}} \tag{4.31}$$

We see that η_{int} is a decreasing function of $j - j_{\text{th}}$ (Figure 4.17).

The output optical power is of the form

$$P = \frac{\hbar\omega}{e} S(j - j_{\text{th}})\eta_{\text{int}} \frac{\beta}{\beta + \alpha_{\text{int}}} \tag{4.32}$$

where β and α_{int} are the mirror and the internal losses, respectively. Thus, the output power is sublinear in the injection current (Figure 4.9). This mechanism of nonlinearity is inherent to quantum-confined lasers of arbitrary dimensionality. Equation (4.31) for η_{int} is universal—it retains the same form for QD, QWR, and QW lasers.

For a given $j - j_{\text{th}}$, the internal quantum efficiency (Figure 4.12) and the output power are controlled by the dimensionless parameter $j_{\text{capt, th}}/j_{\text{th}}^{\text{OCL}}$, which is the ratio of the recombination current in the reservoir to carrier capture current, both taken at threshold. The lower this ratio, the closer η_{int} is to unity (Figure 4.12) and the more linear the LCC (Figure 4.9). Ideally, when this ratio vanishes (e.g., when $j_{\text{th}}^{\text{OCL}} = 0$—no recombination in the OCL), one has $\eta_{\text{int}} = 1$ at an arbitrary injection current and the LCC is linear. In general, however, $j_{\text{th}}^{\text{OCL}}$ is a tangible fraction of the total j_{th}, and $\eta_{\text{int}} < 1$ even at $j = j_{\text{th}}$. In optimizing the structure for minimum j_{th}, it is this component that should be suppressed first and foremost [30].

The conclusion that the power performance of a laser is linked to its threshold characteristics is of great importance. The higher the excess of the injection current over the threshold current, the stronger this relation is manifested (Figures 4.9, 4.12, and 4.17). The higher the required output power, the lower should be the threshold current (Figures 4.9, 4.12, and 4.17). Since QD lasers possess the lowest j_{th} among all current semiconductor lasers, these results suggest their other potential advantage, namely the possibility of achieving highest output powers.

The higher the excess current $j - j_{\text{th}}$, the larger the fraction of it that goes into the parasitic recombination outside the active region. To accommodate carrier consumption by the active region, carriers accumulate in the OCL much in excess of their threshold amount. The resultant superlinear increase in parasitic recombination degrades the LCC.

Thus, at high injection currents the LCC is strongly sublinear (Figure 4.9); n and P increase as $\sqrt{j - j_{\text{th}}}$ (Figures 4.17 and 4.9), while η_{int} decreases as $1/\sqrt{j - j_{\text{th}}}$ (Figure 4.17):

$$\eta_{int} = \frac{j_{capt,\ th}}{\sqrt{j_{th}^{OCL}(j - j_{th})}} \tag{4.33}$$

$$n = n_{th}\sqrt{\frac{j - j_{th}}{j_{th}^{OCL}}} \tag{4.34}$$

$$P = \frac{\hbar\omega}{e} S j_{capt,\ th}\sqrt{\frac{j - j_{th}}{j_{th}^{OCL}}}\frac{\beta}{\beta + \alpha_{int}} \tag{4.35}$$

These square root dependences result from the assumed bimolecular ($\propto n^2$) recombination in the OCL.

The higher the degree of superlinearity of the recombination rate in the OCL with respect to n, the higher the degree of sublinearity of the LCC. Because the nonradiative Auger recombination rate increases as n^3, this recombination channel becomes dominant at sufficiently high injection currents. In the Auger limit, the difference $j^{OCL} - j_{th}^{OCL}$ in (4.28) will be dominated by the cubic (in j_{stim}) term, that is, $j - j_{th} \propto j_{stim}^3$. Hence, both j_{stim} and P will be proportional to $\sqrt[3]{j - j_{th}}$ and $\eta_{int} = j_{stim}/(j - j_{th}) \propto j_{stim}/j_{stim}^3 = 1/j_{stim}^2 \propto 1/(j - j_{th})^{2/3}$.

Thus, the actual shape of the nonlinear LCC depends on the dominant recombination channel outside the active region. It is therefore possible to identify the dominant channel by analyzing the LCC shape.

Capture into the Active Region

The ratio $j_{th}^{OCL}/j_{capt,\ th}$ in (4.31) can be written as follows:

$$\frac{j_{th}^{OCL}}{j_{capt,\ th}} = \frac{\tau_{capt,\ th}}{\tau_{th}^{OCL}} \tag{4.36}$$

where the time constants

$$\tau_{th}^{OCL} = \frac{1}{Bn_{th}} \tag{4.37}$$

$$\tau_{capt} = \frac{b}{v_{capt}} = \frac{\tau_{capt,\ 0}}{1 - f_n} \tag{4.38}$$

may be regarded, respectively, as the recombination time in the OCL at the lasing threshold and the "capture time" into the active region; f_n is the level occupancy in the active region at the lasing threshold. (As already discussed, f_n is pinned above threshold.)

The time constant $\tau_{\text{capt},0}$ is the "capture time" into an empty active region. For a QD ensemble,

$$\tau_{\text{capt},0} = \frac{1}{\sigma_n v_n \dfrac{N_S}{b}} \tag{4.39}$$

For a specific structure considered in [38, 39], $\tau_{\text{capt},0} = 10^{-10}$ sec.

With (4.38), the stimulated recombination current density and the output power can be written in the form

$$j_{\text{stim}} = \frac{eb(n - n_{\text{th}})}{\tau_{\text{capt}}} \tag{4.40}$$

$$P = \hbar\omega \frac{V_{\text{OCL}}(n - n_{\text{th}})}{\tau_{\text{capt}}} \frac{\beta}{\beta + \alpha_{\text{int}}} \tag{4.41}$$

where V_{OCL} is the OCL volume. Equations (4.40) and (4.41) reflect the obvious fact that the supply of carriers to the active region (the origin of all stimulated photons and optical power) occurs by the capture process.

For both nonlinear recombination channels in the OCL, either spontaneous radiation, or nonradiative Auger recombination, $\tau_{\text{th}}^{\text{OCL}}$ depends on n_{th} (as $\tau_{\text{th}}^{\text{OCL}} \propto 1/n_{\text{th}}$ or $1/n_{\text{th}}^2$, respectively). The "capture time" τ_{capt} is inversely proportional to the 3D density of unoccupied states in the QD ensemble $(N_S/b)(1 - f_n)$. Both f_n and n_{th} depend on the structure parameters (see Section 4.4.7). For this reason, $\tau_{\text{th}}^{\text{OCL}}$ and τ_{capt} are not the true time constants describing the respective processes. Further still, τ_{capt} is a characteristic of the entire QD ensemble, rather than of a single QD. In the strict sense, the capture time into a single QD cannot be introduced properly (though this is sometimes done in the literature). The adequate physical quantity, describing correctly the carrier capture into a single QD, is the capture cross section σ_n.

4.4.7 Critical Sensitivity to Structure Parameters

As discussed earlier, the modal gain is limited by its saturation value $g^{\max}$ [see (4.3)]. This implies that lasing in QD structures is possible only in a certain range of tolerable parameters. This range is given by the inequality $g^{\max}[N_S, (\Delta\varepsilon)_{\text{inhom}}] \geq \beta(L)$ (Figure 4.18). The boundary of the tolerable region (the surface $g^{\max} = \beta$ in Figure 4.18) determines the critical tolerable parameters of the structure—the minimum surface density of QDs $N_S^{\min}$, the maximum rms of relative QD size fluctuations $\delta^{\max}$ and the minimum cavity length $L^{\min}$ [30, 37]:

$$N_S^{\min} = \frac{4}{\xi}\left(\frac{\sqrt{\varepsilon}}{\lambda_0}\right)^2 \tau_{\text{QD}} \frac{(\Delta\varepsilon)_{\text{inhom}}}{\hbar} \frac{a}{\Gamma} \frac{1}{L} \ln\frac{1}{R} \tag{4.42}$$

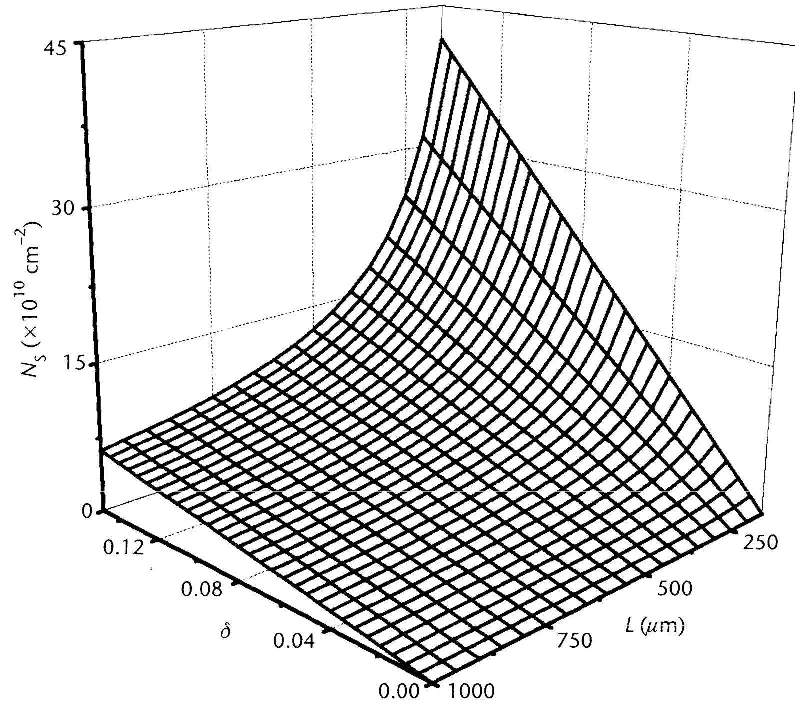

Figure 4.18 Tolerable values of structure parameters. The three axes correspond to the surface density of QDs, the rms of relative QD size fluctuations, and the cavity length. The range of tolerable values of these parameters lies above the shown surface. (*From:* [37]. © 2000 IEEE. Reprinted with permission.)

$$\delta^{\max} = \frac{\xi}{4}\left(\frac{\lambda_0}{\sqrt{\varepsilon}}\right)^2 \frac{1}{\tau_{\text{QD}}} \frac{\Gamma}{a} \frac{\hbar}{\left(q_n \varepsilon_n + q_p \varepsilon_p\right)} \left(\ln \frac{1}{R}\right)^{-1} L N_s \tag{4.43}$$

$$L^{\min} = \frac{4}{\xi}\left(\frac{\sqrt{\varepsilon}}{\lambda_0}\right)^2 \tau_{\text{QD}} \frac{a}{\Gamma} \frac{(\Delta\varepsilon)_{\text{inhom}}}{\hbar} \frac{1}{N_S} \ln \frac{1}{R} \tag{4.44}$$

where R is the facet reflectivity.

The more perfect the structure (lower δ) or the longer the cavity, the lower is $N_S^{\min}$. The denser the QD ensemble (the greater N_S) or the longer the cavity, the greater is $\delta^{\max}$. The more perfect the structure or the denser the QD ensemble, the shorter is $L^{\min}$.

The threshold condition can be expressed [37] in terms of the critical parameters as follows:

$$f_n + f_p - 1 \frac{\delta}{\delta^{\max}} \tag{4.45}$$

Equation (4.45) describes the population inversion in a mean-sized QD required for the lasing at a given δ. The ratio δ / δ^{max} on the right side of (4.45) [and, similarly, (4.9)] can be equivalently replaced by N_S^{min} / N_S or L^{min} / L.

The fact that lasing is possible only for a certain range of structure parameters is inherent to all types of lasers. This is of particular importance for QD lasers in view of the great variability of their structure parameters (such as N_S and δ). In a well-designed QD laser, all parameters should be far away from their critical values.

Threshold Characteristics

Equation (4.45) shows that as a structure parameter approaches its critical value ($N_S \to N_S^{min}$, or $\delta \to \delta^{max}$, or $L \to L^{min}$, both f_n and f_p tend to unity. This means that both the electron and the hole QD levels become fully occupied, which requires infinitely high free-carrier densities in the OCL [see (4.7) and (4.10)] and hence infinitely high pumping: $j_{th} \to \infty$ [see (4.11) and Figure 4.5].

Multimode Generation Threshold

As any structure parameter approaches its critical value, one sees the divergence of not only the threshold current density for the main mode j_{th} but also of the threshold current density for the next mode j_2 and of the multimode generation threshold δj [see (4.14) and Figure 4.5]. At the same time, the relative multimode generation threshold $\delta j / j_{th}$ drops to zero (see the insets in Figure 4.5), which means an infinite increase in the number of simultaneously generated longitudinal modes.

Power Characteristics

The level occupancy in a QD at the lasing threshold ranges within $1/2 < f_n < 1$ [here we assume QD charge neutrality and use (4.9)]. The low value of 1/2 corresponds to a vanishing QD size dispersion or negligible total loss, when the lasing threshold is close to the transparency threshold.

As discussed earlier [see (4.31)], reducing $j_{th}^{OCL} / j_{capt,\,th}$ is a key to enhancing the internal quantum efficiency and the output power. The minimum value of this ratio (obtained when $f_n = 1/2$) is typically much less than unity. Thus, for a specific structure considered in [38, 39], it is 10^{-3} at room temperature.

When the structure parameter is close to its critical value, then $f_n \to 1$ and $j_{th}^{OCL} / j_{capt,\,th} \to \infty$. As a result, the internal quantum efficiency and the output power both drop to zero (Figure 4.8).

In view of the critical dependence of the ratio $j_{th}^{OCL} / j_{capt,\,th}$ on structure parameters, it is crucial to optimize the QD laser design. Thus, for the optimized structure considered in [38, 39] ($f_n^{opt} = 0.655$), this ratio is 3×10^{-3}, which is close to its minimum value. This means that the LCC of such an optimized structure will be linear up to very high injection currents (Figure 4.19).

Critical structure parameters for threshold and power characteristics also exist in QWR and QW lasers.

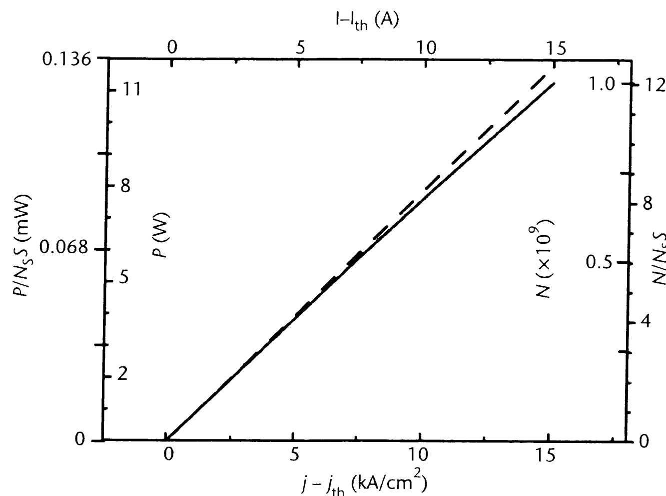

Figure 4.19 Injection current density dependence of the output power (left axis) and photon number (right axis) for a broad-area ($W = 100$ μm) optimized QD laser ($N_S^{opt} = 8.268 \times 10^{10}$ cm^{-2}, $b^{opt} = 0.227$ μm, and $j_{th} = 12.41$ A/cm^2). The dashed line corresponds to the ideal situation, $\eta_{int} = 1$. Power and photon number per QD are also shown. The top axis shows the excess injection current. (*From:* [39]. © 2003 IEEE. Reprinted with permission.)

4.4.8 Dependence of the Maximum Gain on the QD Shape

The maximum modal gain of a laser g^{max} depends on the shape of QDs [47, 48] and it is higher for more symmetrical QDs. It should therefore be possible to improve the laser performance by engineering optimal QD shapes. The crucial factor is the overlap integral I between the electron and the hole wave functions, which strongly affects g^{max} [$g^{max} \propto I$, see (4.3) and (4.4)]. Ideally, in QDs of highly symmetrical (e.g., cubic) shape, this integral is close to unity and the spontaneous radiative lifetime τ_{QD} is about 1 ns or shorter. In this case, the saturation value of the modal gain g^{max} for a single layer of QDs is a few tens of cm^{-1}, which is high enough to ensure lasing even in short (submillimeter) cavities. The actual self-organized QDs are of lower symmetry (e.g., pyramidal shape) and the overlap integral between the ground electron and hole states is several times less than unity [45]. This makes g^{max} as low as several cm^{-1} [47, 48] and lasing in short cavities becomes impossible. Clearly, it would be of tremendous value to control the shape of self-organized QDs.

Recently, a method was developed to grow more symmetrical (truncated) QDs [28]. A laser diode with truncated QDs outperformed a reference sample with nontruncated, pyramidal QDs. The authors demonstrated almost a factor of 2 increase in g^{max} and an extremely high $T_0 = 380$K (at temperatures up to 55°C). This is the highest value of T_0 ever reported in this temperature range.

An alternative technique of shape-engineering was developed in [62], based on controlling the QD heights. These authors also demonstrated a significant change in the optical properties of their structures.

4.4.9 Internal Optical Loss

Internal optical loss adversely affects operating characteristics of semiconductor lasers. Because of the lower value of the optical confinement factor, the effect of internal loss is stronger for lasers with a reduced-dimensionality active region, such as QW, QWR, and QD lasers, than for bulk lasers [10].

All different processes, contributing to the internal loss, can be grouped into two categories, one (such as free-carrier-absorption in the OCL, or simply the waveguide) dependent on the injection carrier density, the other (such as interface scattering or absorption in the cladding layers) insensitive to this density [63]. Absorption in the active region of QW and QWR lasers is relatively small compared to absorption in the OCL, at least at high injection currents j (or high temperatures T—see [64, 65]); the analogous process in the active region of QD lasers, which is carrier photoexcitation from the discrete levels to the continuous-spectrum states, is also small [30, 66]. Neglecting these processes, we must be concerned only with the free-carrier density n in the OCL. Therefore, we need a relation between n and the occupancy of states in the quantum-confined active region, involved in the lasing transition. At sufficiently high temperatures and below the lasing threshold, this relation is given by equilibrium statistics and is of the form of (4.7).

Assuming equal electron and hole occupancies ($f_n = f_p$) and writing the total net internal loss coefficient α_{int} (the quantity we shall refer to simply as the *internal loss*) as the sum of a constant α_0 and a component linear in n, the lasing threshold condition is brought into the form [63] [see (4.1)]:

$$g^{max}(2f_n - 1) = \beta + \alpha_0 + \sigma_{int} n_1 \frac{f_n}{1 = f_n} \tag{4.46}$$

where g^{max} is the maximum (saturation) value of the modal gain $g^m(f_n) = g^{max}(2f_n - 1)$ [see (4.2)], β is the mirror loss, and $\sigma_{int} = \text{const}(n)$ can be viewed as an effective cross section for all absorption loss processes (for the type of carrier that dominates absorption).

The solutions of (4.46) are [Figure 4.20(a)]

$$f_{n1,n2} = f_n^{crit} \mp \sqrt{\left(f_n^{crit}\right)^2 - f_{n0} - \frac{1}{2}\frac{\alpha_0}{g^{max}}} \tag{4.47}$$

where

$$f_n^{crit} + \frac{1}{2}\left(1 + f_{n0} + \frac{1}{2}\frac{\alpha_0}{g^{max}} - \frac{1}{2}\frac{\sigma_{int} n_1}{g^{max}}\right) \tag{4.48}$$

is the "critical" solution [when the cavity length equals its minimum tolerable value—see (4.53) later] and

$$f_{n0} = \frac{1}{2}\left(1 + \frac{\beta}{g^{\max}}\right) \tag{4.49}$$

is the solution in the absence of internal loss; (4.49) is an equivalent representation of (4.9).

Both solutions (4.47) are physically meaningful and describe two distinct lasing thresholds [63]. The lower solution, f_{n1}, is the conventional threshold, similar to f_{n0} but modified by α_{int}. The second solution, f_{n2}, appears purely as a consequence of the carrier density-dependent α_{int} in the OCL.

In the absence of lasing, the injection current density has the following relation to f_n [30, 39]:

$$j = \frac{eN_S}{\tau_{\text{QD}}} f_n^2 + ebBn_1^2 \frac{f_n^2}{(1-f_n)^2} \tag{4.50}$$

The lower and the upper threshold current densities, j_{th1} and j_{th2}, are given by (4.50) wherein one substitutes either $f_n = f_{n1}$ or $f_n = f_{n2}$.

The existence of a second lasing threshold stems from the nonmonotonic dependence of $g^{\text{m}} - \alpha_{\text{int}}$ on f_n [Figure 4.20(a)], or, equivalently, on n or j [Figure 4.20(b)]. The point is that the modal gain $g^{\text{m}}(f_{\text{n}}) = g^{\max}(2f_{\text{n}} - 1)$ increases linearly with f_{n} [Figure 4.20(a)] and saturates at its maximum value $g^{\max}$ as $f_n \to 1$ [which corresponds to $n \to \infty$ and $j \to \infty$—see (4.7), (4.50), and Figure 4.20(b)]. At the same time, α_{int} is superlinear in f_n [see (4.46) and Figure 4.20(a)] and increases infinitely as $f_n \to 1$. At a certain f_n, that is, at a certain j, the rate of increase in α_{int} with j will inevitably equal that of increase in g^{m}, and hence the difference $g^{\text{m}} - \alpha_{\text{int}}$ will peak. Any further increase of j will decrease the difference $g^{\text{m}} - \alpha_{\text{int}}$ [see Figure 4.20(b)]. This corresponds to the so-called "loss-multiplication" regime, discussed in [64, 65] for QW lasers (and attributed to the pileup of carriers due to electrostatic band-profile deformation [44, 67]) and in [68, 69] for QD lasers. As evident from our analysis, this regime and the second lasing threshold are inherent to all structures where α_{int} depends on n.

Note that the second lasing threshold can also arise due to other mechanisms, for example, carrier heating. As the carrier temperature increases with j [9, 44, 70–72], the modal gain itself can become a nonmonotonic function of j, decreasing at high j [70, 71].

In a CW operation, increasing j from zero, one reaches the first lasing threshold j_{th1}. Above this threshold, the difference between the gain and the internal loss is pinned at the value of the mirror loss β and hence Figure 4.20 (which is valid for determining the positions of both thresholds) no longer applies. What actually happens above j_{th1} is shown in Figure 4.21, derived by rigorously solving the rate equations in the presence of light generation [63].

Above the second threshold j_{th2} and up to a maximum current $j_{\max}$, both the gain-current dependence [Figure 4.21(a)] and the LCC [Figure 4.21(b)] are two-valued. At $j = j_{\max}$, the two branches merge in both characteristics. The origin of this striking

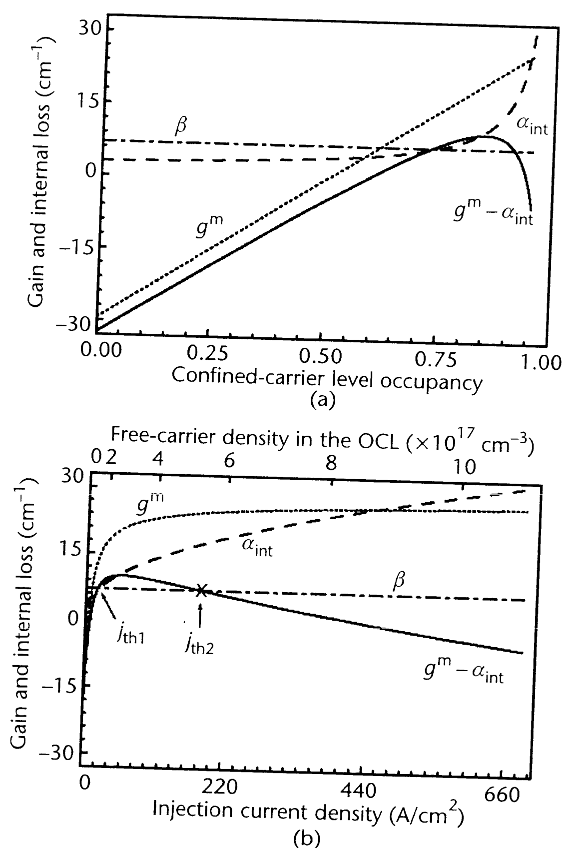

Figure 4.20 Illustration of the threshold condition (4.46) and the two lasing thresholds. Modal gain $g^{m} = g^{max}(2f_n - 1)$ [inclined dotted line in (a) and dotted curve in (b)], internal loss $\alpha_{int} = \alpha_0 + \sigma_{int}\, n = \alpha_0 + \sigma_{int}\, n_1\, f_n / (1 - f_n)$ (dashed curve) and difference of modal gain and internal loss (solid curve) against confined-carrier level occupancy in the active region f_n (a), free-carrier density in the OCL n [(b), top axis] and injection current density j [(b), bottom axis]. The intersections of the solid curve and the horizontal dash-dotted line for the mirror loss $\beta = (1/L)\ \ln\ (1/R)$ define the solutions (4.47) of (4.46). We assume a GaInAsP/InP-based QD heterostructure lasing near 1.55 μm [30, 39] with 10% QD size fluctuations and $N_S = 6.11 \times 10^{10}$ cm^{-2} (for these parameters, g^{max} = 29.52 cm^{-1}). At T = 300 K, $n_1 = 5.07 \times 10^{16}$ cm^{-3}. The mirror loss β = 7 cm^{-1}. Parameters α_0 and s_{int} are plausibly taken as 3 cm^{-1} and 2.65 × 10^{-17} cm^{-1}, respectively. (*From:* [63]. © 2003 American Institute of Physics. Reprinted with permission.)

behavior is clear. As α_{int} increases with the current, the gain strictly follows it so as to maintain the stable generation condition $g^{m} - \alpha_{int} = \beta$. This continues up to the maximum pump current j_{max} at which the lasing is quenched.

At this time, we cannot propose a definite experimental technique to access the lower branch of the LCC [Figure 4.21(b)]. (Analysis of the stability of the lower branch regime will be published elsewhere.) Nevertheless, we stress that an experimental determination of the second threshold would provide us with a new and valuable technique for measuring the loss parameters. Indeed, with the measured j_{th1} and j_{th2}, the values of f_{n1} and f_{n2} can be calculated from (4.50). Both α_0 and σ_{int} can then be expressed in terms of f_{n1} and f_{n2} as follows [see (4.47) and (4.48)]:

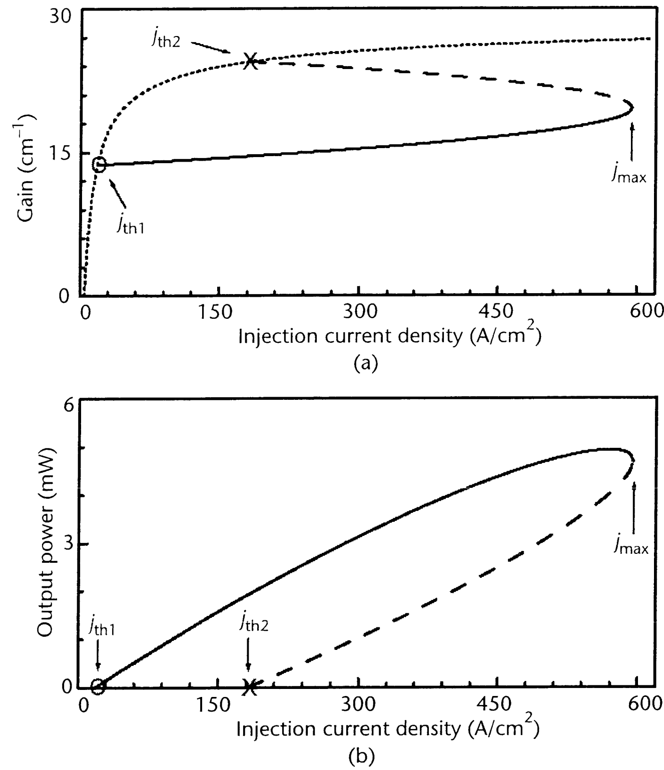

Figure 4.21 Two-valued characteristics: (a) gain-current and (b) light-current. The branches corresponding to the lower and upper lasing regimes (solid and dashed curves, respectively) merge together at the point j_{max} which defines the maximum operating current. At $j > j_{max}$, the lasing is quenched. The dotted curve in (a) is the gain-current dependence for a nonlasing regime; the intersection of the solid (dashed) curve and the dotted curve determines j_{th1} (j_{th2}). In (b), the assumed stripe width $w = 2\ \mu$m. (*From:* [63]. © 2003 American Institute of Physics. Reprinted with permission.)

$$\alpha_0 = 2g^{\max}\left(f_{n1}f_{n2} - f_{n0}\right) \tag{4.51}$$

$$\sigma_{\text{int}} = 2\frac{g^{\max}}{n_1}\left(1 + f_{n1}f_{n2} - f_{n1} - f_{n2}\right) \tag{4.52}$$

When only one threshold exists, the carrier density-dependent internal loss is negligible and α_0 is determined from the "–" solution in (4.47).

The thresholds j_{th1} and j_{th2} depend on the cavity length L (Figure 4.22) and approach each other as L decreases. At a certain critical L that we shall call the minimum tolerable cavity length L^{min}, the horizontal line for the mirror loss β is tangent to the curve for $g^m - \alpha_{int}$ at its maximum (Figure 4.20). In this case, the threshold condition has only one solution, her $f_{n1} = f_{n2} = f_n^{crit}$, and $j_{th1} = j_{th2}$. For $L < L^{min}$, there is no solution of the threshold condition and hence no lasing is possible. The equation for L^{min} is

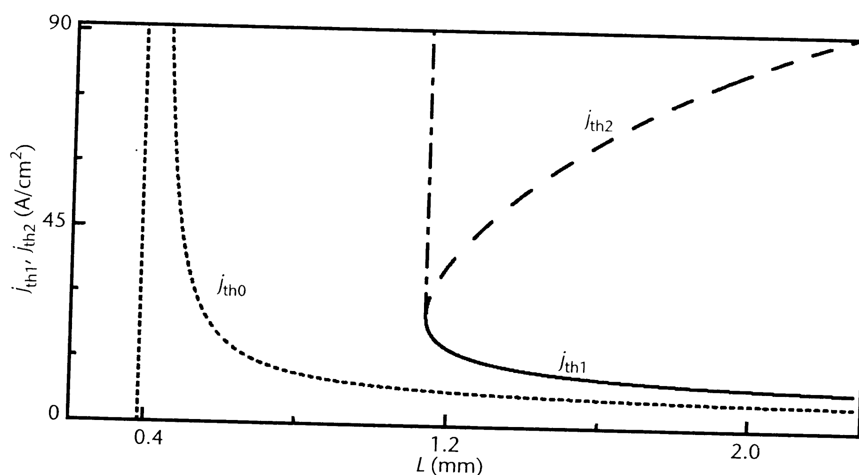

Figure 4.22 The lower and upper threshold current densities (solid and dashed curves, respectively), j_{th1} and j_{th2}, against L. The curve for j_{th1} joins smoothly the vertical dash-dotted line at the critical point. The dotted curve and the vertical dotted line show the threshold current density j_{th0} and its asymptote at the critical point in the absence of internal loss. (*From:* [63]. © 2003 American Institute of Physics. Reprinted with permission.)

$$L^{min} = \frac{L_0^{min}}{\left(\sqrt{2} - \sqrt{\frac{\sigma_{int} n_1}{g^{max}}}\right)^2 - 1 - \frac{\alpha_0}{g^{max}}} \tag{4.53}$$

where $L_0^{min} = (1/g^{max}) \ln (1/R)$ is the minimum cavity length in the absence of α_{int} given by (4.44). In (4.48), $\beta^{max} = (1/L^{min}) \ln (1/R)$ should be entered for β in this case.

Measurement of L^{min} provides yet another way of determining the internal loss parameters. For example, L^{min} can be measured for two structures characterized by different mirror reflectivities with other parameters invariant. With these two values of L^{min}, (4.53) will give a set of two equations for α_0 and α_{int}.

Note that L^{min} sets a considerably more stringent restriction than L_0^{min}. Thus, for a QD laser similar to that considered in [30, 39] and taking plausible values $\alpha_0 = 3$ cm^{-1} and $\sigma_{int} = 2.65 \times 10^{-17}$cm^{-1}, we find the maximum tolerable mirror loss to be $\beta^{max} = 10$ cm^{-1}. Assuming as-cleaved facet reflectivity at both ends ($R = 0.32$), this yields $L^{min} = 1.139$ mm, which is almost a threefold increase compared to $L_0^{min} = 386\ \mu$m. Hence, the absence of lasing often observed in short-cavity QD structures can be attributed to the internal loss. This conclusion is consistent with the discussion in [68, 69].

All equations and analysis of this section apply equally to QW, QWR, and QD lasers. One specifies the type of laser by substituting the relevant expression for g^{max} and the appropriate relation between the spontaneous radiative recombination current density in the quantum-confined active region and f_n [30, 39].

4.5 Novel Designs of QD Lasers with Improved Threshold and Power Characteristics

4.5.1 Temperature-Insensitive Threshold

At relatively high temperatures, the dominant source of the T dependence of j_{th} in all semiconductor lasers originates from carriers that do not contribute to the lasing transition. In lasers with 3D (bulk) or 2D (QW) active regions, there is always a population of carriers within some range around the lasing transition energy (Figure 4.14). These carriers reside in the active region itself and their recombination contributes to a T-dependent threshold.

It is the absence of parasitic recombination in the active medium itself that gave rise to the original hopes of ultra-high-temperature stability in QD lasers, where optical transitions occur between discrete levels. However, as discussed earlier, in all conventional QD laser designs the problem of parasitic recombination has not been removed. This recombination arises primarily from carriers residing in the OCL. When the entire injection current is consumed in QDs ($j_{th} = j_{QD}$), the remaining contributions to the T dependence come from (1) recombination in nonlasing QDs [see (4.13)], (2) recombination via nonlasing, excited states in QDs [see (4.21)], and (3) violation of charge neutrality in QDs [see (4.20)]. In this case, there should be only a slight T dependence of j_{th}, and T_0 should be very high.

Thus, we can expect that suppression of the OCL recombination alone will result in a dramatic improvement of the temperature stability.

Tunneling-Injection QD Laser

One way of suppressing the OCL recombination is based on the idea of tunneling injection of carriers into the QDs [36]. Basically, a tunneling-injection QD laser is a separate confinement double heterostructure (Figure 4.23). Electrons and holes are injected from n- and p-cladding layers, respectively. The QD layer, located in the central part of the OCL, is clad on both sides by QWs separated from the QDs by thin barrier layers. Injection of carriers into QDs occurs by tunneling from the QWs.

A fraction of injected carriers might not recombine in QDs but escape in a second tunneling step into the "foreign" QW and recombine with the majority carriers there. The size of this fraction depends on the ratio of the escape tunneling rate to the QD recombination rate and is practically independent of T. Clearly, the escape tunneling does not lead to a T dependence of j_{th}.

The key idea of the tunneling-injection device is that carriers cannot bypass the QDs on their way from one QW to another. This means that QDs become the sole reservoir delivering minority carriers to the adjacent QW and OCL regions on either side. Hence, outside the QDs there will be no region in the structure where both electron and hole densities are simultaneously high. The electron density is high where the hole density is negligible, and vice versa. Only in the QDs themselves will there be a nonvanishing spontaneous radiative recombination rate. The suppressed parasitic components of j_{th} would otherwise give the main contribution to temperature dependence.

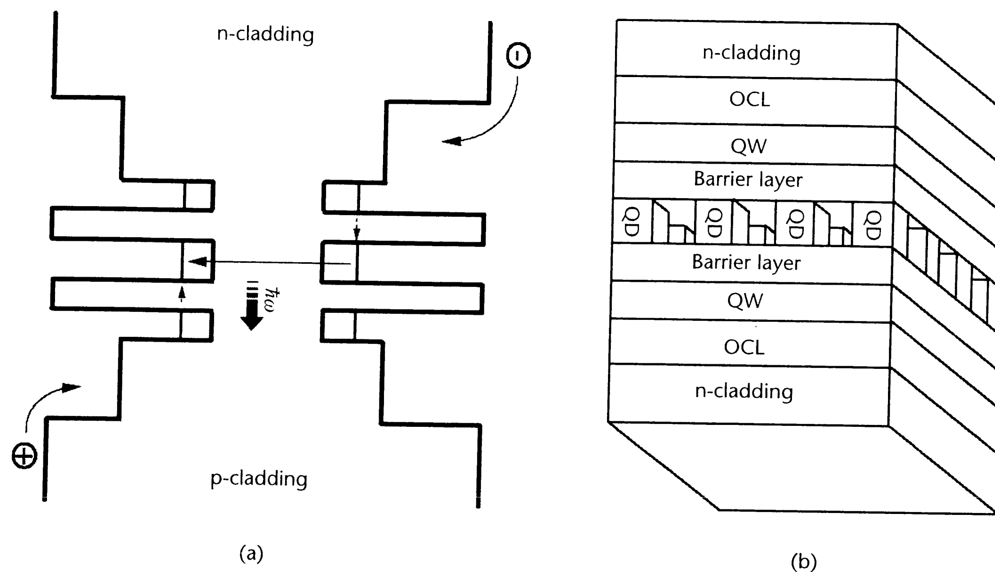

Figure 4.23 (a) Energy band diagram of a tunneling-injection QD laser and (b) schematic view. The QWs and the QDs (not drawn to scale) are assumed implemented in the same material, although this does not necessarily have to be the case in general. The electron-injecting QW is wider than the hole-injecting QW and both QWs are narrower than the QD to accomplish resonant alignment of the majority-carrier subbands with the QD energy levels. The tunnel barrier on the electron-injecting side is made thicker to suppress the leakage of holes from the QD. *(From:* [36]. © 2001 IEEE. Reprinted with permission.)

With the parasitic recombination outside QDs suppressed, there may be only a slight T dependence of $j_{th} = j_{QD}$ arising from the remaining contributions items (1)–(3) listed earlier.

Moreover, it is interesting to note that even these remaining contributions are strongly suppressed in the idealized structure (Figure 4.23) due to the resonant nature of tunneling injection. These "finer" effects discussed later further enhance the temperature stability. In an idealized structure, we can expect a literally infinite T_0.

First, the resonant nature of tunneling injection leads to an effective narrowing of the inhomogeneous linewidth. Indeed, such mechanism of injection inherently selects the QDs of the "right" size, since it requires the confined-carrier levels to be in resonance with the lowest subband states in the QW. When this condition is met by the QDs of average size, the number of active QDs will be maximized. Selective injection means that nonlasing QDs are not pumped at all. Second, the tunneling injection selectively removes the supply of carriers to the nonlasing excited states in a lasing QD. Third, the resonant nature of tunneling injection favors correlation of the QD occupancies by electrons and holes, so that all active QDs will tend to remain neutral.

It is encouraging to note recent developments related to the concept of a tunneling-injection QD laser. In [72–74], a CW room temperature (both photo-pumped and diode) lasing was demonstrated in the InAlP–In(AlGa)P–InP visible-

red system (λ = 656–679 μm), wherein the InP QDs were coupled by resonant tunneling to a single InGaP QW. In the later work [75, 76], this idea was realized in the AlGaAs–GaAs–InGaAs–InAs infrared system, wherein the InAs QDs were coupled to the InGaAs QWs. In contrast to [72–74], the QD layer in [75, 76] was sandwiched between the two QWs; like the structure in Figure 4.23(b), the QWs were of different thickness. The use of tunnel coupling of QDs to QW(s) improved the carrier collection and localization in the QD region and reduced j_{th}. In [77], the tunneling transition rate from a QW to a model (disk-shaped) QD was calculated. In [78], introducing the tunnel-injector QW from only the n-side of the structure increased significantly T_0 of the InGaAs/GaAs QD laser (T_0 = 237K at room temperature). In [79], T_0 = 363K was reported in the temperature range of 278 to 333K, and T_0 = 202K in the temperature range 333 to 373K.

Bandgap-Engineered QD Laser

Tunneling injection suppresses parasitic recombination by ensuring that the electron density is high where the hole density is negligible, and vice versa. An alternative approach to accomplish this goal can be based on the ability to independently control the potential barriers and fields acting on electrons and holes in the same physical region [49].

In the structures in Figure 4.24, the QD layer is embedded in the OCL in such a way that there are only low barriers [Figure 4.24(a)] or no barrier at all [Figure 4.24(b)] for injection of electrons (from the left) and holes (from the right) into the QDs. On the other hand, the structures are provided with large impenetrable escape barriers that block electron injection into the right-hand side of the structure, where holes are majority carriers, and hole injection into the left-hand side of the structure, where electrons are in abundance. Heterostructure barriers as in Figure 4.24(a) can readily be found within the manifold of quaternary III–V heterojunctions, both strained and lattice matched. The structure in Figure 4.24(b) is a limit case, which serves to illustrate that no barrier for injected carriers is necessary on the injecting side.

The space within the QD layer between the QDs can comprise either of the two barriers or be implemented as a wider gap semiconductor that blocks both carrier types.

In contrast to the ideal tunneling-injection QD laser, the three remaining minor sources (1)–(3) of temperature dependence will "survive" in bandgap-engineered QD lasers. Nevertheless, suppression of the main mechanism alone will make such lasers practically temperature insensitive.

4.5.2 Enhanced Power Performance

The radically new design strategy, proposed to improve the temperature stability of QD lasers [36, 49] and discussed in Section 4.5.1, will also enhance the power characteristics. Inasmuch as the two reservoirs feeding carriers into the QDs are essentially unipolar, the finite-delay capture process is not accompanied by a buildup of bipolar carrier density and no additional recombination occurs. We can therefore

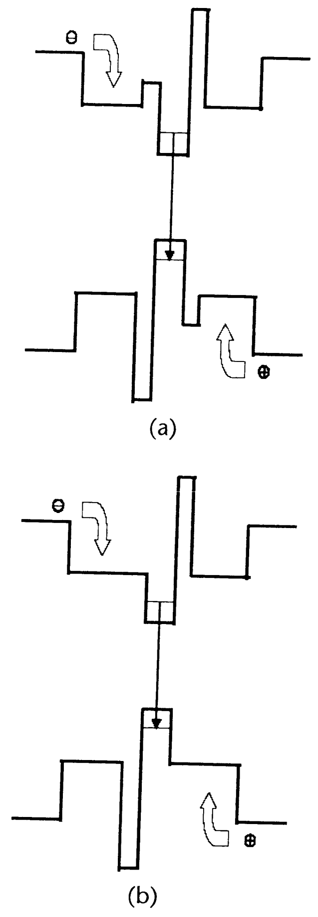

Figure 4.24 (a, b) Bandgap-engineered QD laser structures. The QDs (shown with energy levels) are clad by heterostructure barrier layers that block only the minority carrier transport. (*From:* [49]. © 2003 IEEE Reprinted with permission.)

expect that lasers designed according to [36, 49] will exhibit linear behavior and excellent power performance.

4.6 Other Perspectives

The QD lasers reviewed so far in this chapter are all edge-emitting lasers with Fabry-Perot cavities. Also, they are all based on interband (bipolar) optical transitions. Some feasible alternatives are briefly discussed next.

Vertical cavity surface-emitting lasers (VCSELs) are of high interest for optical signal transmission. The VCSEL's active medium is embedded in a short λ cavity and a single longitudinal mode operation is automatically realized. To keep the loss low, both mirrors should be highly reflective. They are usually realized as stacks of

$\lambda/4$ distributed Bragg reflectors. The vertical cavity represents a one-dimensional microcavity. Using a narrow QD ensemble with the transition energy matched to the cavity passband, optimum photon and electron control can be achieved at a low j_{th}. Due to carrier localization in QDs, also their spreading out of the injection region can be suppressed. This may result in ultralow threshold currents (<70 μA) at ultrasmall apertures (submicrometer). The use of InGaAs QDs in GaAs-based VCSELs emitting at 1.3 μm [80]—the wavelength especially important for single-mode fiber communication—presents one of the most apparent and successful applications of QDs.

A VCSEL based on a single QD is also possible to fabricate. In such a laser, the inhomogeneous broadening, inherent to QD ensembles, will be absent. A single QD VCSEL will be a semiconductor analog of a single atom laser [81] or an ion trap laser [82].

Another promising direction is to use QDs in unipolar (intraband) semiconductor lasers. In these lasers, stimulated emission comes from the transitions between states of carriers in the same band [83, 84]. This concept was realized in the unipolar *quantum cascade laser* (QCL) [85, 86]. Transition energies in unipolar lasers can be tailored to suit important applications at mid- and far-infrared wavelengths.

All contemporary unipolar lasers suffer from a fundamental problem associated with an extremely low efficiency of intraband optical transitions: The optical transition rate in the best QCLs is 3.5 orders of magnitude lower than the nonradiative relaxation rate due to phonon emission. This problem is inherent to transitions between the continuous-spectrum states of overlapping subbands and it cannot be completely eliminated in QW unipolar lasers. As a consequence, CW room temperature operation of such lasers requires very high j_{th}.

The use of QDs offers a radical solution to this problem, based on the discrete carrier spectrum in QDs. The phonon relaxation will be completely suppressed if the energy of optical transitions (both direct transitions between electron levels in a given QD and indirect transitions between electron levels in neighboring QDs) is detuned from the LO phonon energy. The amount of detuning should be greater than the phonon energy dispersion. Because the energy levels in a QD can be varied in a wide range (by controlling the size of QDs and the band offsets between the constituent materials), such control is quite feasible. The nonradiative single-phonon relaxation will thus be practically suppressed. As a rule, the multiple-phonon relaxation rate is much lower than that of single-phonon relaxation and it is usually negligible. The idea for using QDs in unipolar lasers was proposed in [87–93].

Finally, instead of the Fabry-Perot cavity assumed so far, one may be interested in using *distributed feedback* (DFB) [10, 60] for certain applications that need stabilizing in the single-mode generation. Due to a difference in the refraction index of the QD and the surrounding region, a spatially periodic arrangement of QDs [94] will give rise to a sufficient periodic index variation for an index-coupled DFB. At the same time, the periodic arrangement of active QDs provides a spatially periodic variation of the gain. This may provide the benefits of the so-called gain-coupling scheme, without any phase shifter or antireflection coating [95–100].

References

[1] Zory, Jr., P. S., (ed.), *Quantum Well Lasers*, Boston, MA: Academic Press, 1993.

[2] Kapon, E., (ed.), *Semiconductor Lasers*, San Diego, CA: Academic Press, 1999.

[3] Bimberg, D., M. Grundmann, and N. N. Ledentsov, *Quantum Dot Heterostructures*, New York: John Wiley & Sons, 1999.

[4] Dingle, R., and C. H. Henry, *Quantum Effects in Heterostructure Lasers*, U.S. Patent 3982207, September 21, 1976.

[5] van der Ziel, J. P., et al.,"Laser Oscillations from Quantum States in Very Thin GaAs-$Al_{0.2}Ga_{0.8}As$ Multilayer Structures," *Appl. Phys. Lett.*, Vol. 26, No. 8, 1975, pp. 463–465.

[6] Dupuis, R. D., "Room Temperature Operation of Quantum-Well $Ga_{1-x}Al_xAs$-GaAs Laser Diodes Grown by Metalorganic Chemical Vapor Deposition," *Appl. Phys. Lett.*, Vol. 32, No. 5, 1978, pp. 295–297.

[7] Tsang, W. T., "Extremely Low Threshold (AlGa)As Graded-Index Waveguide Separate-Confinement Heterostructure Lasers Grown by Molecular-Beam Epitaxy," *Appl. Phys. Lett.*, Vol. 40, No. 3, 1982, pp. 217–219.

[8] Arakawa, Y., and H. Sakaki, "Multidimensional Quantum Well Laser and Temperature Dependence of Its Threshold Current," *Appl. Phys. Lett.*, Vol. 40, No. 11, June 1982, pp. 939–941.

[9] Eliseev, P. G., *Introduction to the Physics of Injection Lasers*, Moscow, Russia: Nauka, 1983 (in Russian).

[10] Agrawal, G. P., and N. K. Dutta, *Long-Wavelength Semiconductor Lasers*, New York: Van Nostrand Reinhold Company, 1986.

[11] Alferov, Z., "Double Heterostructure Lasers: Early Days and Future Perspectives," *IEEE J. Select. Topics Quantum Electron.*, Vol. 6, No. 6, November/December 2000, pp. 832–840.

[12] Asada, M., Y. Miyamoto, and Y. Suematsu, "Gain and the Threshold of Three-Dimensional Quantum-Box Lasers," *IEEE J. Quantum Electron.*, Vol. 22, No. 9, September 1986, pp. 1915–1921.

[13] Vahala, K. J., "Quantum Box Fabrication Tolerance and Size Limits in Semiconductors and Their Effect on Optical Gain," *IEEE J. Quantum Electron.*, Vol. 24, No. 3, March 1988, pp. 523–530.

[14] Miyamoto, Y., et al., "Threshold Current Density of GaInAsP/InP Quantum-Box Lasers," *IEEE J. Quantum Electron.*, Vol. 25, No. 9, September 1989, pp. 2001–2006.

[15] Alferov, Z. I., and R. F. Kazarinov, "Semiconductor Laser with Electric Pumping," Inventor's Certificate 181737, Application 950840, priority as of March 30, 1963 (in Russian).

[16] Alferov, Z. I., et al., "AlAs-GaAs Heterojunction Injection Lasers with a Low Room-Temperature Threshold," *Sov. Phys. Semicond.*, Vol. 3, No. 9, September 1970, pp. 1107–1110.

[17] Alferov, Z. I., et al., "Investigation of Influence of AlAs-GaAs Heterostructure Parameters on Laser Threshold Current and Realization of Continuous Emission at Room Temperature," *Sov. Phys. Semicond.*, Vol. 4, No. 9, September 1971, pp. 1573–1575.

[18] Hayashi, I., et al., "Junction Lasers Which Operate Continuously at Room Temperature," *Appl. Phys. Lett.*, Vol. 17, No. 3, 1970, pp. 109–111.

[19] Ekimov, A. I. and A. A. Onushchenko, "Quantum Size Effect in 3-Dimensional Microscopic Semiconductor Crystals," *JETP Lett.*, Vol. 34, No. 6, 1981, pp. 345–349.

[20] Ledentsov, N. N., et al., "Optical Properties of Heterostructures with InGaAs-GaAs Quantum Clusters," *Semicond.*, Vol. 28, No. 8, August 1994, pp. 832–834.

[21] Kirstädter, N., et al., "Low Threshold, Large T_0 Injection Laser Emission from (InGa)As Quantum Dots," *Electron Lett.*, Vol. 30, No. 17, August 1994, pp. 1416–1417.

[22] Goldstein, L., et al., "Growth by Molecular Beam Epitaxy and Characterization of InAs/GaAs Strained-Layer Superlattices," *Appl. Phys. Lett.*, Vol. 47, No. 10, November 1985, pp. 1099–1101.

[23] Shchukin, V. A., N. N. Ledentsov, and D. Bimberg, *Epitaxy of Nanostructures*, Berlin, Germany: Springer, 2003.

[24] Maximov, M. V., et al., "Gain and Threshold Characteristics of Long Wavelength Lasers Based on InAs/GaAs Quantum Dots Formed by Activated Alloy Phase Separation," *IEEE J. Quantum Electron.*, Vol. 37, No. 5, May 2001, pp. 676–683.

[25] Park, G., et al., "Low-Threshold Oxide-Confined 1.3-μm Quantum-Dot Laser," *IEEE Phot. Technol. Lett.*, Vol. 13, No. 3, March 2000, pp. 230–232.

[26] Shchekin, O. B., and D. G. Deppe, "1.3 μm InAs Quantum Dot Laser with T_0 = 161K from 0 to 80 μm C," *Appl. Phys. Lett.*, Vol. 80, No. 18, May 2002, pp. 3277–3279.

[27] Kovsh, A. R., et al., "InAs/InGaAs/GaAs Quantum Dot Lasers of 1.3 μm Range with High (88%) Differential Efficiency," *Electron. Lett.*, Vol. 38, No. 19, September 2002, pp. 1104–1106.

[28] Tokranov, V., et al., "Enhanced Thermal Stability of Laser Diodes with Shape-Engineered Quantum Dot Medium," *Appl. Phys. Lett.*, Vol. 83, No. 5, August 2003, pp. 833–835.

[29] Varangis, P. M., et al., "Low-Threshold Quantum Dot Lasers with 201nm Tuning Range," *Electron. Lett.*, Vol. 36, No. 18, August 2000, pp. 1544–1545.

[30] Asryan, L. V., and R. A. Suris, "Inhomogeneous Line Broadening and the Threshold Current Density of a Semiconductor Quantum Dot Laser," *Semicond. Sci. Technol.*, Vol. 11, No. 4, April 1996, pp. 554–567.

[31] Asryan, L. V., and R. A. Suris, "Linewidth Broadening and Threshold Current Density of Quantum-Box Laser," *Proc. of Int. Symp. Nanostructures: Physics and Technology*, St. Petersburg, Russia, June 20–24, 1994, pp. 181–184.

[32] Suris, R. A., and L. V. Asryan, "Quantum-Dot Laser: Gain Spectrum Inhomogeneous Broadening and Threshold Current," *Proc. of SPIE*, Vol. 2399, 1995, pp. 433–444.

[33] Kane, E. O., "Band Structure of Indium Antimonide," *J. Phys. Chem. Solids*, Vol. 1, No. 4, 1957, pp. 249–261.

[34] Evtikhiev, V. P., et al., "Continuous Stimulated Emission at T = 293K from Separate-Confinement Heterostructure Diode Lasers with One Layer of InAs Quantum Dots Grown on Vicinal GaAs(001) Surfaces Misoriented in the [010] Direction in the Active Region," *Semicond.*, Vol. 32, No. 12, December 1998, pp. 1323–1327.

[35] Asryan, L. V., and R. A. Suris, "Temperature Dependence of the Threshold Current Density of a Quantum Dot Laser," *IEEE J. Quantum Electron.*, Vol. 34, No. 5, May 1998, pp. 841–850.

[36] Asryan, L. V., and S. Luryi, "Tunneling-Injection Quantum-Dot Laser: Ultrahigh Temperature Stability," *IEEE J. Quantum Electron.*, Vol. 37, No. 7, July 2001, pp. 905–910.

[37] Asryan, L. V., and R. A. Suris, "Longitudinal Spatial Hole Burning in a Quantum-Dot Laser," *IEEE J. Quantum Electron.*, Vol. 36, No. 10, October 2000, pp. 1151–1160.

[38] Asryan, L. V., S. Luryi, and R. A. Suris, "Intrinsic Nonlinearity of the Light-Current Characteristic of Semiconductor Lasers with a Quantum-Confined Active Region," *Appl. Phys. Lett.*, Vol. 81, No. 12, September 2002, pp. 2154–2156.

[39] Asryan, L. V., S. Luryi, and R. A. Suris, "Internal Efficiency of Semiconductor Lasers with a Quantum-Confined active Region," *IEEE J. Quantum Electron.*, Vol. 39, No. 3, March 2003, pp. 404–418.

[40] Ledentsov, N. N., et al., "Direct Formation of Vertically Coupled Quantum Dots in Stranski-Krastanow Growth," *Phys. Rev. B*, Vol. 54, No. 12, September 1996, pp. 8743–8750.

[41] Pankove, J. I., "Temperature Dependence of Emission Efficiency and Lasing Threshold in Laser Diodes," *IEEE J. Quantum Electron.*, Vol. 4, No. 4, April 1968, pp. 119–122.

[42] Asryan, L. V., and R. A. Suris, "Charge Neutrality Violation in Quantum Dot Lasers," *IEEE J. Select. Topics Quantum Electron.*, Vol. 3, No. 2, April 1997, pp. 148–157.

[43] Tsui, E. S.-M., P. Blood, and A. I. Kucharska, "Charge Neutrality in Quantum-Well Structures," *Semicond. Sci. Technol.*, Vol. 5, No. 4, April 1990, pp. 333–339.

[44] Asryan, L. V., "Threshold Characteristics of InGaAsP/InP Multiple Quantum Well Lasers," *Semicond. Sci. Technol.*, Vol. 15, No. 12, December 2000, pp. 1131–1140.

[45] Stier O., M. Grundmann, and D. Bimberg, "Electronic and Optical Properties of Strained Quantum Dots Modeled by 8-Band $\mathbf{k} \cdot \mathbf{p}$ Theory," *Phys. Rev. B*, Vol. 59, No. 8, February 1999, pp. 5688–5701.

[46] Shoji, H., et al., "Lasing Characteristics of Self-Formed Quantum-Dot Lasers with Multistacked Dot Layer," *IEEE J. Select. Topics Quantum Electron.*, Vol. 3, No. 2, April 1997, pp. 188–195.

[47] Asryan, L. V., et al., "Effect of Excited-State Transitions on the Threshold Characteristics of a Quantum Dot Laser," *IEEE J. Quantum Electron.*, Vol. 37, No. 3, March 2001, pp. 418–425.

[48] Asryan, L. V., et al., "Maximum Modal Gain of a Self-Assembled InAs/GaAs Quantum-Dot Laser," *J. Appl. Phys.*, Vol. 90, No. 3, August 2001, pp. 1666–1668.

[49] Asryan, L. V., and S. Luryi, "Temperature-Insensitive Semiconductor Quantum Dot Laser," *Solid-State Electron.*, Vol. 47, No. 2, February 2003, pp. 205–212.

[50] Statz, H., C. L. Tang, and J. M. Lavine, "Spectral Output of Semiconductor Lasers," *J. Appl. Phys.*, Vol. 35, No. 9, September 1964, pp. 2581–2585.

[51] Alam, M. A., "Effects of Carrier Transport on *L–I* Characteristics of QW Lasers in the Presence of Spatial Hole Burning," *IEEE J. Quantum Electron.*, Vol. 33, No. 6, June 1997, pp. 1018–1024.

[52] Tang, C. L., H. Statz, and G. deMars, "Spectral Output and Spiking Behavior of Solid-State Lasers," *J. Appl. Phys.*, Vol. 34, No. 8, August 1963, pp. 2289–2295.

[53] Suris, R. A., and S. V. Shtofich, "Multifrequency Stimulated Emission from Injection Semi-Conductor Lasers," *Soviet Phys. Semicond.*, Vol. 16, No. 7, July 1982, pp. 851–853.

[54] Suris, R. A., and S. V. Shtofich, "Role of Impurities in the Appearance of Multifrequency Emission from Injection Semiconductor Lasers," *Soviet Phys. Semicond.*, Vol. 17, No. 7, July 1983, pp. 859–861.

[55] Sugawara, M., K. Mukai, and Y. Nakata, "Light Emission Spectra of Columnar-Shaped Self-Assembled InGaAs/GaAs Quantum-Dot Lasers: Effect of Homogeneous Broadening of the Optical Gain on Lasing Characteristics," *Appl. Phys. Lett.*, Vol. 74, No. 11, March 1999, pp. 1561–1563.

[56] Garbuzov, D. Z., et al., "Experimental and Theoretical Investigations of Singularities of the Threshold and Power Characteristics of InGaAsP/InP Separate-Confinement Double-Heterostructure Lasers (λ = 1.3 μm)," *Sov. Phys. Semicond.*, Vol. 25, No. 5, May 1991, pp. 560–564.

[57] Tessler, N., "Nonequilibrium Effects in Quantum Well Lasers," *Appl. Phys. Lett.*, Vol. 61, No. 20, November 1992, pp. 2383–2385.

[58] Hirayama, H., et al., "Estimation of Carrier Capture Time of Quantum-Well Lasers by Spontaneous Emission Spectra," *Appl. Phys. Lett.*, Vol. 61, No. 20, November 1992, pp. 2398–2400.

[59] Hirayama, H., et al., "Carrier Capture Time and Its Effect on the Efficiency of Quantum-Well Lasers," *IEEE J. Quantum Electron.*, Vol. 30, No. 1, January 1994, pp. 54–62.

[60] Coldren L. A., and S. W. Corzine, *Diode Lasers and Photonic Integrated Circuits*, New York: John Wiley & Sons, 1995.

[61] Smowton, P. M., and P. Blood, "The Differential Efficiency of Quantum-Well Lasers," *IEEE J. Select. Topics Quantum Electron.*, Vol. 3, No. 2, April 1997, pp. 491–498.

[62] Kim, J. S., et al., "Structural and Optical Properties of Shape-Engineered InAs Quantum Dots," *J. Appl. Phys.*, Vol. 94, No. 4, August 2003, pp. 2486–2490.

[63] Asryan, L. V., and S. Luryi, "Two Lasing Thresholds in Semiconductor Lasers with a Quantum-Confined Active Region," *Appl. Phys. Lett.*, Vol. 83, No. 26, December 2003, pp. 5368–5370.

[64] Seki, S., et al., "Dominant Mechanisms for the Temperature Sensitivity of 1.3 μm InP-Based Strained-Layer Multiple-Quantum-Well Lasers," *Appl. Phys. Lett.*, Vol. 67, No. 8, August 1995, pp. 1054–1056.

[65] Seki, S., et al., "Dominant Mechanism for Limiting the Maximum Operating Temperature of InP-Based Multiple-Quantum-Well Lasers," *J. Appl. Phys.*, Vol. 79, No. 5, March 1996 pp. 2192–2197.

[66] Asryan, L. V., and R. A. Suris, "Carrier Photoexcitation from Levels in Quantum Dots to States of the Continuum in Lasing," *Semicond.*, Vol. 35, No. 3, March 2001, pp. 343–346.

[67] Seki, S., and K. Yokoyama, "Electrostatic Deformation in Band Profiles of InP-Based Strained-Layer Quantum-Well Lasers," *J. Appl. Phys.*, Vol. 77, No. 10, May 1995, pp. 5180–5184.

[68] Zhukov, A. E., et al., "Loss Multiplication in a Quantum Dot Laser," *Laser Phys.*, Vol. 13, No. 3, March 2003, pp. 319–323.

[69] Kovsh, A. R., et al., "InAs/InGaAs/GaAs Quantum Dot Lasers of 1.3 μm Range with Enhanced Optical Gain," *J. Cryst. Growth*, Vol. 251, Nos. 1–4, April 2003, pp. 729–736.

[70] Gorfinkel, V. B., S. Luryi, and B. Gelmont, "Theory of Gain Spectra for Quantum Cascade Lasers and Temperature Dependence of their Characteristics at Low and Moderate Carrier Concentrations," *IEEE J. Quantum Electron.*, Vol. 32, No. 11, November 1996, pp. 1995–2003.

[71] Gorfinkel, V., M. Kisin, and S. Luryi, "Hot Electrons and Curves of Constant Gain in Long Wavelength Quantum Well Lasers," *Optics Express*, Vol. 2, No. 4, February 1998, pp. 125–130.

[72] Asryan, L. V., et al., "High-Power and High-Temperature Operation of InGaAsP/InP Multiple Quantum Well Lasers," *Semicond. Sci. Technol.*, Vol. 14, No. 12, December 1999, pp. 1069–1075.

[73] Walter, G., et al., "Room-Temperature Continuous Photopumped Laser Operation of Coupled InP Quantum Dot and InGaP Quantum Well InP-InGaP-In(AlGa)P-InAlP Heterostructures," *Appl. Phys. Lett.*, Vol. 79, No. 13, September 2001, pp. 1956–1958.

[74] Walter, G., et al., "Coupled InP Quantum-Dot InGaP Quantum Well InP-InGaP-In(AlGa)P-InAlP Heterostructure Diode Laser Operation," *Appl. Phys. Lett.*, Vol. 79, No. 20, November 2001, pp. 3215–3217.

[75] Chung, T., G. Walter, and N. Holonyak, Jr., "Coupled Strained-Layer InGaAs Quantum-Well Improvement of an InAs Quantum Dot AlGaAs-GaAs-InGaAs-InAs Heterostructure Laser," *Appl. Phys. Lett.*, Vol. 79, No. 27, December 2001, pp. 4500–4502.

[76] Walter, G., T. Chung, and N. Holonyak, Jr., "High-Gain Coupled InGaAs Quantum Well InAs Quantum Dot AlGaAs-GaAs-InGaAs-InAs Heterostructure Diode Laser Operation," *Appl. Phys. Lett.*, Vol. 80, No. 7, February 2002, pp. 1126–1128.

[77] Chuang, S. L., and N. Holonyak, Jr., "Efficient Quantum Well to Quantum Dot Tunneling: Analytical Solutions," *Appl. Phys. Lett.*, Vol. 80, No. 7, February 2002, pp. 1270–1272.

[78] Bhattacharya, P., and S. Ghosh, "Tunnel Injection $In_{0.4}Ga_{0.6}As$/GaAs Quantum Dot Lasers with 15GHz Modulation Bandwidth and T_0 = 237 K at Room Temperature," *Appl. Phys. Lett.*, Vol. 80, No. 19, May 2002, pp. 3482–3484.

[79] Pradhan, S., S. Ghosh, and P. Bhattacharya, "Temperature Dependent Steady-State Characteristics of High-Performance Tunnel Injection Quantum Dot Lasers," *Electron. Lett.*, Vol. 38, No. 23, November 2002, pp. 1449–1450.

[80] Lott, J. A., et al., "InAs-InGaAs Quantum Dot VCSELs on GaAs Substrates Emitting at 1.3 μm," *Electron. Lett.*, Vol. 36, No. 16, August 2000, pp. 1384–1385.

[81] An, K., et al., "Microlaser—A Laser with One-Atom in an Optical-Resonator," *Phys. Rev. Lett.*, Vol. 73, No. 25, December 1994, pp. 3375–3378.

[82] Meyer, G. M., H.-J. Briegel, and H. Walther, "Ion-Trap Laser," *Europhys. Lett.*, Vol. 37, No. 5, February 1997, pp. 317–322.

[83] Kazarinov, R. F., and R. A. Suris, "Possibility of Amplification of Electromagnetic Waves in a Semiconductor with a Superlattice," *Sov. Phys. Semicond.*, Vol. 5, No. 4, 1971, p. 707.

[84] Kazarinov, R. F., and R. A. Suris, "Electric and Electromagnetic Properties of Semiconductors with a Superlattice," *Sov. Phys. Semicond.*, Vol. 6, No. 1, 1972, pp. 120–131.

[85] Faist, J. F., et al., "Quantum Cascade Laser," *Science*, Vol. 264, No. 5158, April 1994, pp. 553–556.

[86] Faist, J., et al., "Quantum Cascade Laser: An Intersub-Band Semiconductor-Laser Operating Above Liquid-Nitrogen Temperature," *Electron. Lett.*, Vol. 30, No. 11, pp. 865–866, May 1994.

[87] Suris, R. A., "Prospects for Quantum Dot Structures Applications in Electronics and Optoelectronics," *Proc. NATO Advanced Research Workshop, Future Trends in Microelectronics: Reflections on the Road to Nanotechnology*, S. Luryi, et al., (eds.), France, July 17–21, 1995, pp. 197–208. (*Also published in NATO ASI Series, Series E: Applied Sciences*, Vol. 323, Dordrecht: Kluwer Academic Publishers, 1996.)

[88] Wingreen, N. S., and C. A. Stafford, "Quantum-Dot Cascade Laser: Proposal for an Ultralow-Threshold Semiconductor Laser," *IEEE J. Quantum Electron.*, Vol. 33, No. 7, July 1997, pp. 1170–1173.

[89] Wingreen, N. S., and C. A. Stafford, "Quantum-Dot Cascade Laser," U.S. Patent 5692003, November 25, 1997.

[90] Wingreen, N. S., "Quantum-Dot Cascade Laser," U.S. Patent 5963571, October 5, 1999.

[91] Singh, J., "Possibility of Room Temperature Intra-Band Lasing in Quantum Dot Structures Placed in High-Photon Density Cavities," *IEEE Photon. Technol. Lett.*, Vol. 8, No. 4, April 1996, pp. 488–490.

[92] Botez, D., P. S. Zory, and C.-F. Hsu, "Intersubband Quantum Box Semiconductor Laser," U.S. Patent 5953356, September 14, 1999.

[93] Hsu, C.-F., et al., "Intersubband Quantum-Box Semiconductor Lasers," *IEEE J. Select. Topics Quantum Electron.*, Vol. 6, No. 3, May/June 2000, pp. 491-503.

[94] Kuramochi, E., J. Temmyo, and T. Tamamura, "Perfect Spatial Ordering of Self-Organized InGaAs/AlGaAs Box-Like Structure Array on GaAs (311) B Substrate with Silicon Nitride Dot Array," *Appl. Phys. Lett.*, Vol. 71, No. 12, September 1997, pp. 1655–1657.

[95] Griesinger, U. A., et al., "Realization of Dot DFB Lasers," *IEEE Photon. Technol. Lett.*, Vol. 8, No. 5, May 1996, pp. 587–589.

[96] Griesinger, U. A., et al., "Fabrication and Investigation of Nanostructures and Their Application in New Laser Devices," *J. Vac. Sci. Technol. B*, Vol. 14, No. 6, November–December 1996, pp. 4058–4061.

[97] Wang, J., et al., "Emission Dynamics of Dot and Wire DFB Lasers," *IEEE Photon. Technol. Lett.*, Vol. 8, No. 12, December 1996, pp. 1585–1587.

[98] Wang, J., U. A. Griesinger, and H. Schweizer, "Intrinsic Carrier Capture Time in Deep-Etched Quantum-Box (70 nm Diameter) Lasers at Low Temperature: An Indication of Extremely High Quantum Capture Efficiency," *Appl. Phys. Lett.*, Vol. 70, No. 9, March 1997, pp. 1152–1154.

[99] Wang, J., et al., "Carrier Capture Times in Quantum-Well, -Wire, and -Box Distributed-Feedback Lasers Characterized by Dynamic Lasing Emission Measurements," *IEEE J. Select. Topics Quantum Electron.*, Vol. 3, No. 2, April 1997, pp. 223–229.

[100] Susa, N., "Feasibility Study on the Application of the Quantum Disk to the Gain-Coupled Distributed Feedback Laser," *IEEE J. Quantum Electron.*, Vol. 34, No. 8, August 1998, pp. 1317–1324.